TECHNISCHE UNIVERSITÄT WIEN
Vienna University of Technology

Diploma Thesis

Phase stability and thermomechanical properties of sputter deposited Ta-C-N coatings

carried out for the purpose of obtaining the degree of Dipl. Ing., submitted at TU Wien, Faculty of Mechanical and Industrial Engineering,

Thomas Glechner, BSc

Mat.Nr.: 01227055
Urban-Loritz-Platz 4/15, 1070 Wien, Austria
under the supervision of

Univ.Prof. Dipl.-Ing. Dr.mont. Paul Heinz Mayrhofer
Univ. Ass. Dipl.-Ing. Dr. Helmut Riedl
Institute of Materials Science and Technology, E308

Wien, April 2018

Affidavit

I declare in lieu of oath, that I wrote this thesis and performed the associated research myself, using only literature cited in this volume.

Date *Signature*

Acknowledgements

First of all, I want to thank Univ. Prof. Paul Heinz Mayrhofer for giving me the opportunity to accomplish this thesis.
Furthermore, I particularly want to thank Dr. Helmut Riedl for his outstanding assistance. Thank you, Helmut, for your investment in me and the great possibilities you gave me during the thesis. I could learn so much from you, and you were always taking time for me and my questions. THANK YOU!

I also want to thank all my colleagues in the thin film group for the great working atmosphere, helpfulness and support in all needs. I really enjoyed working with you!

Special thanks also belong to Associate Prof. Suneel Kodambaka from the University of California Los Angeles, who hosted me for three and a half months, giving me the opportunity to experience research in a foreign country at a great university. Thanks goes also to his whole group, who gave me a worm welcome there.

Last but not least I want to say thank you to my parents and family who always supported me in every need during the whole studies, making it possible for me to stand where I am now. And of course, thank you my beloved Christina for all your support, listening and patience with me during this time.

Table of Contents

Acknowledgements II

Table of Contents III

Abstract IV

Kurzfassung VI

1 Introduction and Motivation 1

2 Ultra-High Temperature Ceramics (UHTC) 1

2.1 Transition metal carbides and nitrides 1

2.2 Transition metal carbonitrides 6

3 Mechanical properties of thin film materials 8

3.1 Fracture toughness evaluation 8

3.2 Ductility of ceramic coatings 13

3.3 Micromechanical testing Methods 14

List of References 19

4 Publications 25

Publication I 26

Publication II 51

5 Concluding remarks 69

Abstract

Exploring novel thin film materials with outstanding mechanical properties – especially, high hardness but simultaneously high damage tolerance – as well as superior temperature stability is for a major goal in the field of protective coating-applications. Therefore, thin film materials such as transition metal (TM) carbides, nitrides, and borides are highly popular in this field. Among all these ceramic thin films, the binary Ta-C system exhibits the highest melting temperature combined with further outstanding properties such as chemical inertness, or high thermal conductivity. However, the extreme brittle behavior of this compound drastically limits the field of use.

Therefore, new concepts such as tailoring thermomechanical properties by substituting carbon with nitrogen atoms is a highly interesting approach, changing the bonding state towards a more metallic like character through non-metals – hence increasing ductility. Based on ab initio calculations we could experimentally proof, that up to a nitrogen content of about 65 % on the non-metallic sublattice, Ta-C-N crystals prevail a face centered cubic structure in sputter deposited thin films. The cubic structures are partly stabilized by both non-metal and Ta vacancies, whereas metal defects are decisive for nitrogen rich compositions. With increasing nitrogen content super-hard fcc-$TaC_{0.71}$ thin films weaken from around 40 GPa to 25 GPa for $TaC_{0.32}N_{0.68}$, respectively, accompanied by a linear decrease in indentation modulus. In accordance with a slightly reduced thermal stability, meaning phase degradation detected around 1300 °C in DSC/TG analysis, this indicates a reduced bonding strength hence a reduced covalent and more metallic like bonding character – confirmed by PDOS. Pugh's semi-empirical criterion for ductility (B/G > 1.75) even suggest ductile behavior with the addition of nitrogen. This finding is confirmed by various micromechanical testing methods on a sputter deposited 110-oriented $Ta_{0.47}C_{0.34}N_{0.19}$ film. Although this film exhibits super-hardness (43.3±1.4 GPa) plastic deformation is observed in micro-pillar compression tests over a yield stress, σ_Y, of 16.89±1.39 GPa with {111} <$01\bar{1}$> as the most active slip system. In addition, single cantilever bending tests result in a stress intensity factor, K_{IC}, of 2.9±0.25 MPa·$m^{1/2}$ whereas pillar splitting tests suggest K_{IC}=7.12±0.8 MPa $m^{1/2}$. Furthermore, superior fracture toughness of $Ta_{0.47}C_{0.34}N_{0.19}$ compared to $TaC_{0.81}$ is proofed by cantilever testing.

This study emphasizes an alternative alloying concept for ceramic like thin film materials, by forming solid solutions on the non-metallic sublattice. The investigated Ta-C-N system gives a promising prospective for further ultra-high temperature ceramics.

Kurzfassung

Carbide und Nitride der frühen Übergangsmetalle sind weit verbreitet als Schutz - und Verschleiß mindernde Schichten aufgrund ihrer hohen Härte und chemischen Beständigkeit. Unter ihnen besitzt Tantal-Carbid (Ta-C) den höchsten Schmelzpunkt sowie weitere außerordentliche Eigenschaften, jedoch den Nachteil hoher Sprödigkeit, die eine breite Anwendung erschweren. In dieser Arbeit wurde daher untersucht, wie durch das Legieren von Nichtmetallen, sprich durch den Austausch von Kohlenstoff mit Stickstoffatomen, die Eigenschaften gezielt verändert werden können um die Duktilität von Ta-C zu verbessern. Die mittels DFT Berechnungen vorhergesagte Erweiterung des fcc-Ta-C-N Einphasenfeldes für höhere Stickstoffgehälter durch Lehrstellen konnte experimentell bis zu einem Stickstoffgehalt von ca. 65 % am Nichtmetall-Untergitter bestätigt werden. Die bevorzugten Leerstellenart variiert dabei mit zunehmender Stickstoffkonzentration.

Mechanische Untersuchungen ergaben, dass die Härte ausgehend von $TaC_{0.71}$ mit steigendem Stickstoffgehalt von ca. 40 GPa auf 25 GPa für $TaC_{0.32}N_{0.68}$ erniedrigt wird. Dasselbe gilt für den gemessenen E-Modul, dessen Verlauf wiederum in guter Übereinstimmung mit den berechneten elastischen Konstanten liegt. Gemeinsam mit einer etwas geringeren thermischen Stabilität, die sich durch einen Massenverlust und einer damit verbunden Phasenzersetzung bei ca. 1300 °C zeigt, sowie berechneten Zustandsdichten, deutet diese Erniedrigung auf eine Abnahme des kovalenten Bindungscharakters und eine verstärkt metallische Binding hin. Das semi-empirische Pugh-Kriterium für Duktilität deutet zusätzlich auf ein vermehrt duktiles Verhalten mit zunehmenden Stickstoff in der Schicht hin. Mikromechanische Versuche an einer 110-texturierten $Ta_{0.47}C_{0.34}N_{0.19}$ Schicht zeigen plastische Verformung trotz einer Härte von 43.3±1.4 GPa. Die Verformung erfolgt dabei hauptsächlich über das {111} $<01\bar{1}>$ Gleitsystem. Es konnte außerdem eine Steigerung der Bruchzähigkeit dieser Schicht im Vergleich zu $TaC_{0.81}$ ermittelt werden.

Dieser Ansatz des Nichtmetall Legierens zeigt nicht nur außerordentliche Eigenschaften für Ta-C-N, sondern ist auch eine vielversprechende Möglichkeit Materialeigenschaften anderer Systeme gezielt zu verbessern.

1 Introduction and Motivation

Transition metal (TM) carbides and nitrides have been subject for intensive research due to their outstanding properties. These material systems exhibit extreme hardness, excellent resistant to wear, oxidation, corrosion, as well as high temperature mechanical strength and excellent thermal and electrical conductivities. Furthermore, they belong to the class of ultra-high temperature ceramics (UHTC) exhibiting highest melting temperatures among all materials available. All these outstanding properties, makes them highly attractive for applications, especially as protective thin films. Among these TM- carbides, Ta-C exhibits the highest melting temperature (3983 °C [1]) and the highest electrical conductivity (> 5 x 10^6 $\Omega^{-1}m^{-1}$ at 300 K [2]). Like other TM carbides, Ta-C also exhibits extreme hardness and chemical inertness due to their predominant covalent bonding character but on the contrary, also low ductility. This drawback limits their application as engineering components as well as thin films.

Compared to other TM carbides a unique mechanical behavior has been observed. It was shown that Ta-C single crystals behave in a relatively ductile manner and deform plastically before cracking during micro indentation at 77K [3]. This was attributed to the activation of a second slip system and furthermore indicates that Ta-C appears to have a still more metallic bonding nature than other TM carbides.

On the other hand, Ta-N, has been subject of intense research due to their application as thin films (as diffusion barriers) in integrated circuits. Besides the good wear resistance [4] and high hardness [5], density functional theory (DFT) calculations suggested cubic Ta-N as ductile [6]. Therefore, combining the carbide and nitride of tantalum with their excellent properties, forming Ta-C-N is very promising approach for obliterating the disadvantage of both binaries. Hereby, the concept of non-metallic alloying on the carbon/nitrogen sublattice and how it can be used to improve material properties is the major motivation for the study of the Ta-C-N system.

Among TM carbonitrides only Ti-C-N has yet been investigated more intensively – reduced friction coefficient and improved wear resistant compared to Ti-N [7] – whereas only little research was conducted on Ta-C-N. A very promising study applying this concept has been done in the theoretical work by Hong and van der Walle [8] for the Hf-C-N system. They proposed that the addition of an additional element from Hf-C to the ternary system of Hf-C-

N leads to an increase of the melting point. From their calculations they suggested, that Hf-C-N with 27 % of Carbon and 20 % of Nitrogen increases the currently highest proposed melting point by 200 K. Furthermore, they suggested the Ta-Hf-C-N system as an even superior candidate with even higher melting points.

In addition to enhancing high temperature stability, decreasing the extreme brittleness of TM carbides and nitrides is highly desired for a variety of applications. Basic mechanisms to increase the ductility of ceramic materials are the incorporation of ductile phases, grain boundary engineering, or varying crystallite and grain sizes. For thin film materials architectural arrangements such as superlattices or hierarchical composites achieved interesting results concerning fracture toughness enhancements [9–10], where K_{IC} increases by one order of magnitude. However, these methods only improve ductility on an extrinsic level. To improve the ductility of the material itself on an intrinsic level, thin film materials design needs to be conducted on the atomic scale range adapting the bonding state [11]. On the goal to achieve more ductile ceramics gaining detailed knowledge of the role of composition, slip systems, crystal anisotropy and structural defects on the deformation behavior is essential [12].

For the determination of mechanical properties of thin films, the use of Focused Ion Beam (FIB) has opened new possibilities on the nano-scale. The compression of FIB-milled pillars has become a widely used method. First conducted by Uchic et al. [13], this method has been applied dominantly on single crystalline materials but also polycrystalline and thin film materials [14–15]. With these tests, insight into the mechanical behavior at very small scales can be gained, which is necessary due to the ongoing device miniaturization, but also into the fundamental deformation processes. It was found for various materials that sample size strongly affects the material strength on the micron and submicron scale [16–17]. Compression tests on Ta-C crystals showed that they undergo plastic shear deformation and the slip systems activated are those with the highest resolved shear stress. We therefore want to expand the knowledge of deformation behavior and mechanical properties to the Ta-C-N system synthesized as thin film.

For the formation of Ta-C-N it has to be considered that Ta-C and Ta-N differ in their most stable structures. In contrast to various TM carbides (e.g. TaC_y, HfC_y, ZrC_y), which are stabilized in the fcc NaCl-prototype ($Fm\bar{3}m$, #225) structure, TaN crystallizes predominantly in hexagonal structure types. Two very similar hexagonal prototypes, ε-TaN (P6/mmm, #191) and π-TaN

($P\bar{6}2m$, #189) are known for TaN, where π-TaN is reported to be the most stable one [18]. In equilibrium state, a transition from π-TaN to fcc structured δ-TaN ($Fm\bar{3}m$, #225) is observed at 1950 °C - according to the phase diagram [19]. In contrast, solid solutions of fcc Ta-C and Ta-N can be already formed at noticeably lower temperatures in correspondence to isothermal sections of the ternary Ta-C-N system [19]. These systems are known for the phase stabilization due to vacancies (e.g. vacancies or Schottky defects). For TaC_y the influence of carbon deficiencies is more decisive as for Ta_yN, where metallic vacancies are crucial [6–20]. For Ta_yN, tantalum vacancies are known to stabilize the cubic structure [21]. Physical vapor deposition (PVD) enables now the accesses of meta-stable phases due to highly limited ad-atom kinetics during film growth (extremely high cooling rates 1013 $K \cdot s^{-1}$) and a pronounced introduction of structural defects, such as point defects. Considering these aspects, a stabilization of fcc structured Ta-C-N by PVD is highly presumable [22].

For a better understanding of the binary TM carbides and nitrides as well as the mechanical behavior of thin films, which we want to improve, these topics are described in more detail in the following chapters.

2 Ultra-High Temperature Ceramics (UHTC)

There are several approaches to define UHTC. The most commonly used, are by temperature or by chemistry. The temperature classification includes materials revealing a melting point above 3000 °C. Therefore, not more than four pure elements (Ta, W, Re, and Os) and only one oxide (ThO_2), meet this definition However, most materials fulfilling also these demands are found in early transition metal-borides, -carbides and -nitrides such as ZrB_2, HfB_2, TaC, ZrC and TiN [23]. Due to the material synthesized in this work we want to discuss the early transition metal carbides and nitrides in the next section.

2.1 Transition metal carbides and nitrides

Transition metal carbides as well as nitrides are known for their high hardness, high wear resistance, chemical inertness and high melting points. The melting points of the carbides are generally higher, compared to those of the corresponding nitrides. Group VI TM-nitrides are not even considered as refractory any more. The bonding nature of TM-carbides and -nitrides is partly covalent, ionic and metallic [24]. Their metallic bonding character leads to more metal-like properties such as a high electrical and thermal conductivity. Furthermore, their composition is often non-stoichiometric. For binary carbides, the carbon sites are dominantly vacant and the carbon content cannot exceed 50%. For binary nitrides, MN_x, both the metal and nitride sublattice can exhibit vacancies which result in sub- ($x<1$) and hyperstoichiometric ($x>1$) compositions, respectively. From the application point of view TiN, TiC, WC and TaC are the most important TM-nitrides/-carbides.

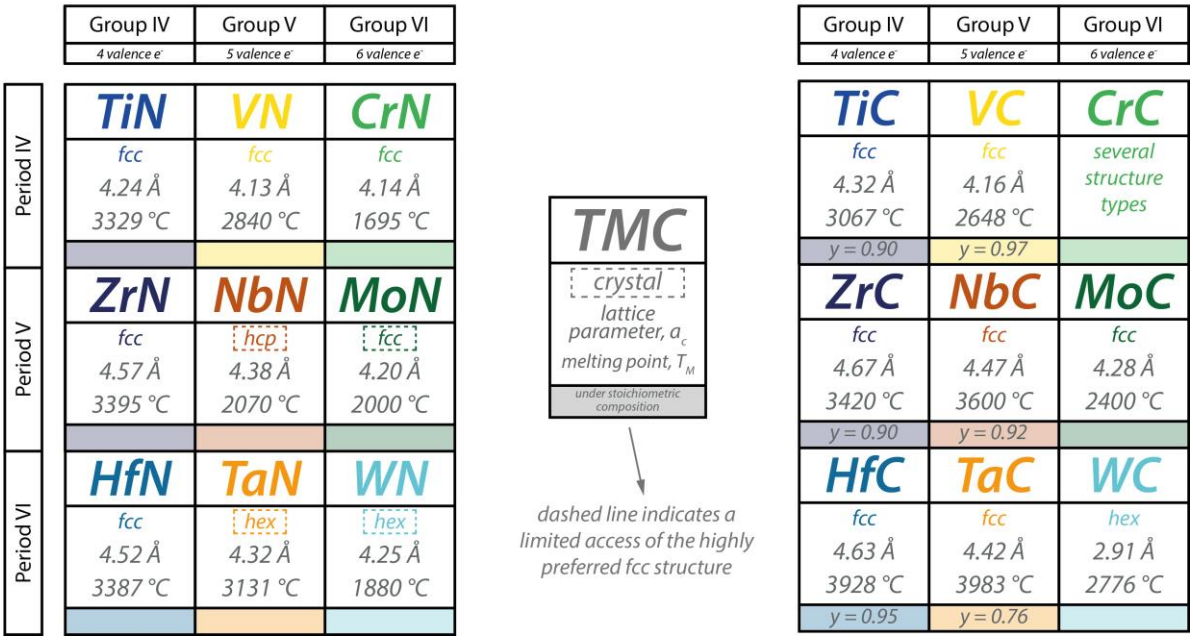

Figure 1: Transition metal carbides and nitrides and their corresponding structure.

2.1.1 Phase formation in transition metal carbides and nitrides

The structure of TM-carbides and –nitrides can be simply described as close packed arrangements of metal atoms with the small non-metal atoms placed on interstitial sites. Therefore, they are often referred to as interstitial carbides, in contrast to covalent carbides and salt-like carbides (carbides formed with elements from different groups in the periodic table). This configuration belongs to the class of intermetallic phases called Hägg-phases after the Swedish chemist Gunnar Hägg. According to him, the structure and preferred interstitial site is dependent on the r_x/r_{Me} ratio, where r_x is the non-metal atom radius and r_{Me} the bigger metal atom radius. For $r_x/r_{Me} \leq 0.59$ simple cubic or hexagonal structures are formed with preferred octahedral site ($0.41 \leq r_x/r_{Me} \leq 0.59$) or tetrahedral site ($r_x/r_{Me} < 0.41$). Except Cr-C all group IV-VI TM carbides and nitrides exhibit an atomic radius ratio of carbon/nitrogen to metal between 0.41 and 0.59. Therefore, metal atoms form simple fcc and hcp, or simple hexagonal substructures, and carbon or nitrogen are placed in the octahedral site [25]. In addition, for most of them there is no carbon-carbon or nitrogen-nitrogen interaction (isolated atoms in the metal matrix) present [25]. Group IV TM-carbides have the lowest r_x/r_{Me} and only form fcc binary carbides (MC) with carbon atoms in all octahedral sites at stoichiometry. The corresponding nitrides form several phases but the major one is again the binary nitride (MN) in its fcc structure. The major most common binary phase of group V TM-carbides on the other hand is the M_2C with half the octahedral sites filled. This composition has hcp structure but

on the contrary, the monocarbides have fcc structure [24]. All carbides of type M_2C have high- and low temperature modifications, which differ only by the arrangement of the carbon atoms on the interstitial positions [26]. The group V nitrides also have hcp M_2N and fcc mononitrides but here the mononitrides have high- and low temperature modifications. At low temperatures VN has tetragonal structure [27], NbN and TaN hcp structure. Group VI TM-carbides as well as nitrides exhibit several different compositions with fcc, hcp and hexagonal structure [24].

A detailed overview of all early binary TM-carbides and –nitrides is given in Figure 1.

2.1.2 Properties of Ta-C and Ta-N

Tantalum is a group V transition metal, which in its pure form, crystallizes in bcc structure. When forming Ta-C or Ta-N, the carbon/nitrogen to metal ratio (r_x/r_{Me}) is 0.53 and 0.51, respectively. The binary tantalum-carbon equilibrium phase diagram is depicted in Figure 3 [28]. The monocarbide, TaC, exhibits fcc rocksalt structure and melts at a temperature of 3983 °C [1]. Ta_2C transforms at 2170 °C, from the low temperature configuration α-Ta_2C ($P\bar{3}m1$ #164), to the high temperature configuration β-Ta_2C ($P6_3/mmc$, #194). For the mononitride TaN two very similar hexagonal prototypes, ε-TaN (P6/mmm, #191) and π-TaN ($P\bar{6}2m$, #189) are known, whereas π-TaN is reported to be the most stable one [18]. In equilibrium state, a transition from π-TaN to fcc structured δ-TaN ($Fm\bar{3}m$, #225) is observed at 1950 °C - according to the phase diagram (Figure 3) [19]. Furthermore, at a r_x/r_{Me}-ratio of 0.33 (Ta_2N) a stable phase can be observed crystallizing in a hexagonal ($P6_3/mmc$ #194) structure. Compared to Ta-N, the corresponding carbide (Ta-C) exhibits a far higher melting temperature and additionally better thermal and electrical conductivity.

In terms of the mechanical properties of Ta-C the compound reveals a significant dependency to the off-stoichiometry composition (TaC_y). R. Hill et. al showed, that the maximum in hardness is obtained for x=0.78 [20]. Ta-C is brittle at room temperature and can be deformed ductile over the fracture appearance transition temperature of about 0.5 T_m. For fcc-Ta-N DFT-calculations of the full elastic tensor predict a very low anisotropy factor [6]. Therefore, crystallographic orientation has a major influence on the hardness. Furthermore, recent

studies [6] also highlighted a ductile behavior of Ta-N. A summary of the various properties of Ta-C and the two Ta-N phases are summarized in Table 1.

Table 1: Summary of properties of Ta-C and Ta-N.

Structural properties	**TaC**	**ε-TaN**	**δ-TaN**
r_x/r_{Me}	0.529	0.508	0.508
Lattice parameter [Å]	4.455 [29]		4.334 [30]
Thermal properties			
Melting temperature [C°]	3983 [1]	-	3093 [24]
Thermal conductivity	22.17	8.78	
Mechanical properties			
Hardness (GPa)	16 [31]	11 [31]	32 (001) [5]
Young's modulus	560 [32]	456 [6]	338 [6]
Physical properties			
Electrical resistivity at RT [μΩ cm]	15 [31]	128 [31]	

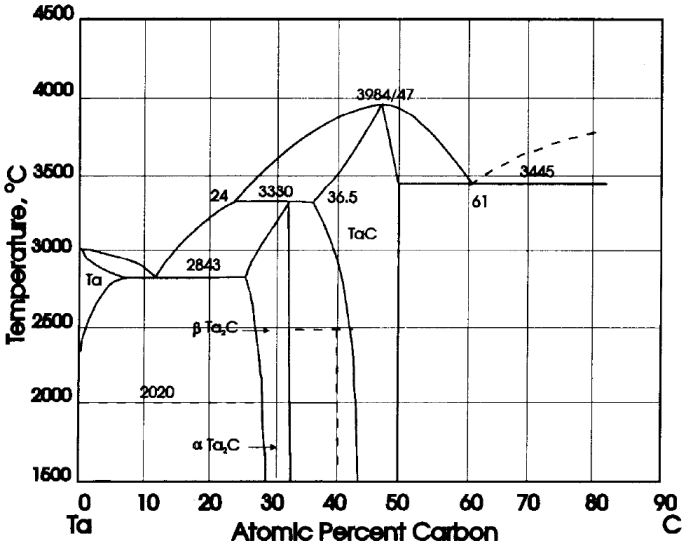

Figure 3: Equilibrium phase diagram of the Ta-C system [24].

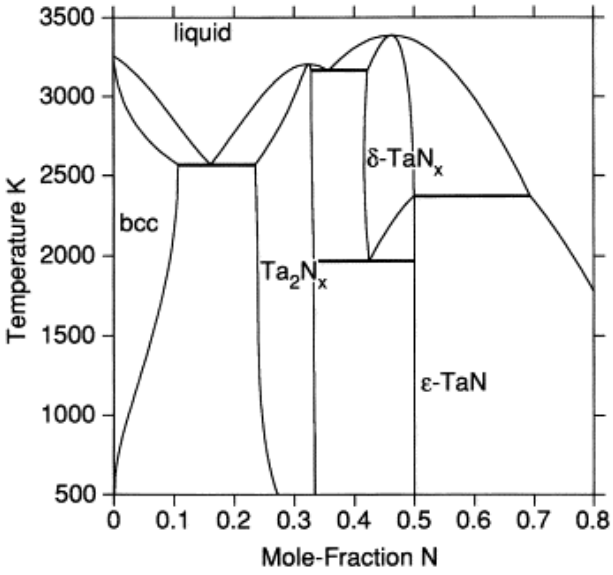

Figure 2: Equilibrium phase diagram of the Ta-N system [19].

2.1.3 Sputter deposition of TM carbides and nitrides

For the deposition of TM carbides and nitrides thin films, various techniques can be applied. Most commonly, chemical vapor deposition- (CVD) and physical vapor deposition- (PVD) processes are used. In this section, the sputter deposition – a PVD process – is discussed. There are two different ways to form nitrides and carbides in a PVD process: reactive and non-reactive sputtering. For TM-nitrides, reactive sputtering is the most commonly used technique. Therefore, the TM-target is sputtered in a reactive gas atmosphere, which is usually a mixture of nitrogen and argon. For carbides, non-reactive sputtering can be done by using a compound target(TM-carbide) or the two pure elemental targets (graphite and metal). In a reactive process, hydrocarbon gas (e.g., acetylene) is used as the carbon source.

According to the TM-C equilibrium phase diagrams (and their corresponding structures) described in section 2.1.1, one would expect different structures depending on the carbon content in the film. Therefore, with increasing carbon content, the M_2C-phases (low carbon content), followed by the monocarbide and ending at a mixture of MC and graphite (high carbon content) should appear. However, due to the non-equilibrium conditions during sputtering, nano-crystallites embedded in an amorphous carbon matrix (a-C) are observed. The crystallites are preferable non-stoichiometric fcc monocarbides. For a certain carbide, the stoichiometry is considered being dependent on the deposition parameters, especially the plasma density near the substrate surface. Furthermore, the process type influences the structure of the a-C phase. Non-reactive sputtering leads to a sp^2 bonded a-C phase whereas the hydrocarbon gases used in reactive sputtering lead to a hydrogen-containing amorphous carbon phase (a-C:H) with a higher content of sp^3 bonds [33]. The MC_x grain size decreases with increasing carbon content and the a-C areas between the grains get larger (see Figure 4) [34].

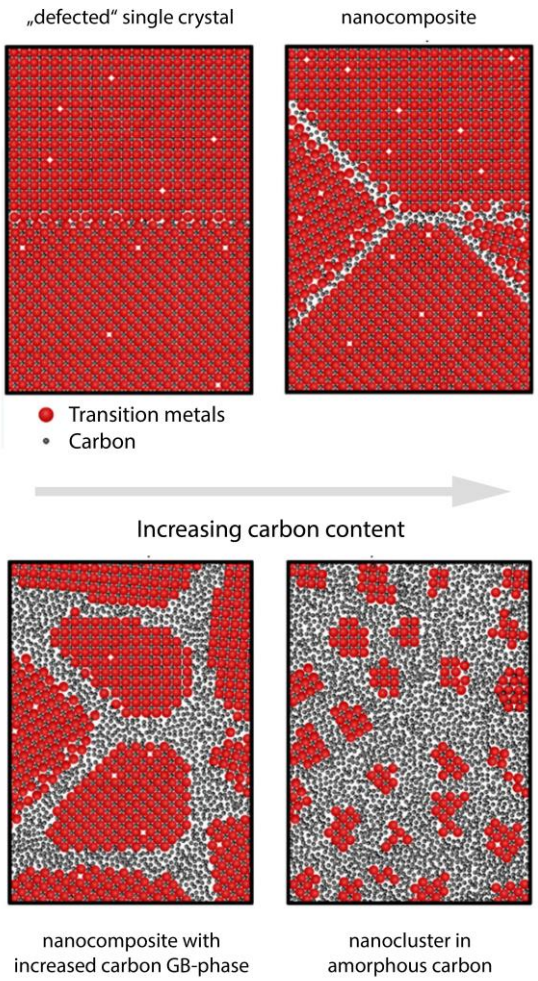

Figure 4: Evolution in the microstructure of sputter deposited TM-carbides [34].

2.2 Transition metal carbonitrides

Most of the transition metal carbides can form a solid solution with their corresponding TM-nitride resulting in TM-carbonitrides. Nitrogen and carbon atoms are of similar size and therefore one species can be substituted completely by the other, without changing the structure of the binary phase. The solid state properties of carbonitrides change with the C/(C+N) ratio und thus offer a large field of tailoring them [31]. Among TM carbonitrides, Ti-C-N is the most common one used for protective coatings due to the reduced friction coefficient and improved wear resistant compared to Ti-N [7]. Group IV transition metal carbonitrides show a dependency of their hardness on the Valence Electron Concentration (VEC). TiC_xN_{1-x} for example has a hardness maximum at about VEC=8.4 [35]. Therefore, with the substitution of carbon atoms with nitrogen on the nonmetal sublattice it is possible to

increase the hardness. In contrast to the group IV carbonitrides, which exhibit a broad solubility of carbide and nitride group V carbonitrides, are completely miscible only at elevated temperatures. This is due to their hexagonal low-temperature configuration of the mononitride.

3 Mechanical properties of thin film materials

3.1 Fracture toughness evaluation

Fracture toughness is used as a measure to describe the material resistance against crack extension. The experimental measurement, evaluation and standardization of fracture toughness plays a very important role due to its high significance as material property in engineering design applications. Structural integrity assessment, damage tolerance design, fitness-for-service evaluation, and residual strength analysis for different engineering components and structures are some of the applications of fracture mechanics [36]. In the following section the concepts of the linear elastic fracture mechanics are described, which is only valid if nonlinear material deformation happens only in a small region surrounding the crack tip [37]. To describe materials with non-linear elastic behavior further theories have to be applied. Nevertheless, for brittle materials, the linear elastic behavior is a good approximation.

3.1.1 Linear elastic fracture mechanics

On an atomic level, fracture in a material means that inter-atomic bonds are broken due to an external applied load. As early as 1920, Griffith formulated his criterion for crack formation or crack growth for an existing crack. Crack growth only occurs when the total energy decreases. This means that the energy resisting the crack growth needs to be overcome. This energy includes surface energy, and plastic work or other type of energy dissipation. Therefore, this approach is also called energy approach.

Griffith criterion: $$\sigma_f = \left(\frac{2E\gamma_S}{\pi a}\right)^{1/2} \qquad (1.1)$$

Equation 1.1 shows the Griffith criterion, where σ_f denotes the failure stress, γ_s the surface energy E the total energy and a half the crack length. Irwin later developed the present version of the energy approach (see Equation 1.2). He defined an energy release rate, G, as the rate

of energy dissipated during fracture with increasing crack area for a linear elastic material. This includes also the absorbed plastic energy.

$$G = \frac{\pi\sigma^2 a}{E} \qquad (1.2)$$

At the moment of fracture $G=G_c$ (critical energy release rate).

When describing the stress state near the tip of a crack (please, see Figure 6), each stress component is proportional to a constant. This constant is called the stress intensity factor K. There are three main modes of loading a crack can experience (or a combination of them) as shown in Figure 5: Mode I loading, where load is applied perpendicular to the crack plane-

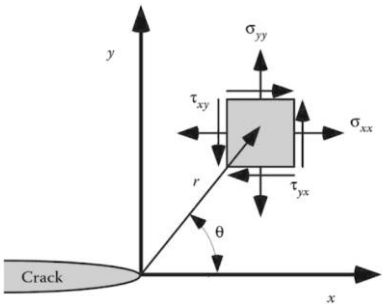

Figure 6: Stress state at crack tip [37].

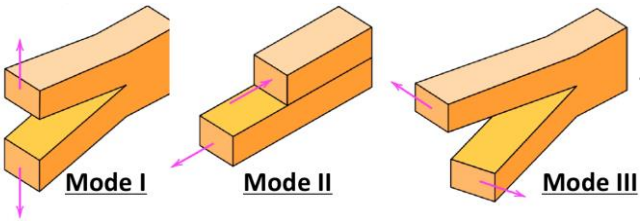

Figure 5: Loading Modes.

Mode II, corresponds to in-plane shear loading -Mode III to out-of-plane shear. K is dependent on the loading mode, which is therefore denoted by a subscript, K_I, K_{II} or K_{III}.

When knowing K, it is possible to calculate the whole stress state at the crack tip as a function of r and θ (r and θ see Figure 6). When additionally taking into account the assumption, that further cracking happens at the crack tip at a certain critical stress-strain state, it follows that a failure happens also at a critical value of the stress intensity factor, K_{IC}. Therefore, this value can be used as a measure of fracture toughness [37].

$$K_{(I,II,III)} = Y\sigma\sqrt{\pi a} \qquad (2)$$

In equation 2, Y denotes a dimensionless constant that depends on geometry and mode of loading.

3.1.2 Fracture toughness testing

As already mentioned before, fracture toughness tests determine the resistance of a material against crack extension. A test may provide a single value of fracture toughness or a resistance curve where a toughness parameter is plotted against crack extension. The toughness parameter is commonly chosen, depending on the material deformation behavior. For brittle materials the specimen often fails unstable, therefore only a single value can be measured (usually K_{IC}). Several standards from different organizations have been developed for fracture toughness measurements. The first standards for K, were developed by the America Society or Testing and Materials (ASTM) in 1970. Most test procedures have common features and the design of test specimens is similar. In many cases of the testing procedure, only load and displacement are measured and recorded, but for some also the evolution of the crack growth is crucial and therefore the crack growth monitored. In general, used specimen configurations are the compact tension (C(T)) and the single-edge notched bend (SE(B)). Each specimen configuration has three important characteristics, including the crack length (a), thickness (B) and width (W) [37]. For testing in the micron range these macroscopic methods are adapted according to the lower scale.

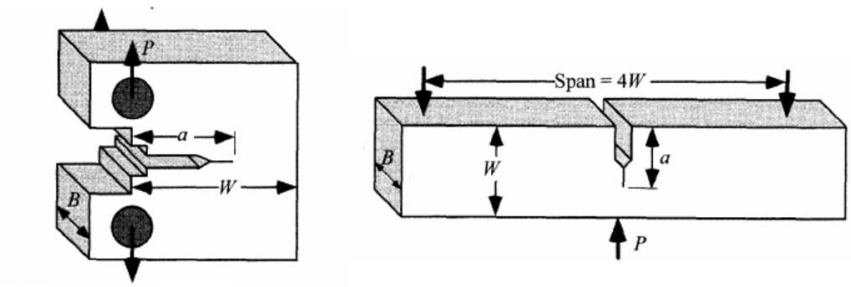

Figure 7: Specimen configuration: left C(T), right SE(B) [37].

3.1.3 Testing methods of thin film materials

For measuring fracture toughness of ceramic thin films several different methods have been proposed, such as single cantilever beam tests, Vickers indentation cracking and pillar splitting [38–39]. In the following section, four different techniques used shall be explained.

3.1.3.1 Vickers indentation cracking techniques

These techniques were among the first proposed due to their advantage of simple testing and sample preparation. A four-sided pyramidal indenter penetrates the surface and produces radial cracks. The fracture toughness can then be extracted by measuring the length of the crack at a certain applied indentation load [38]. Furthermore, different crack morphologies exist, such as median, radial, cone, lateral and half penny cracks. These morphologies as well as the size of the cracks are dependent on material properties, indenter geometry and applied indentation load. Therefore, relating indentation crack length and fracture toughness is a non-trivial task, which can only be done empirically and therefore limits the accuracy and applicability of this method [40].

3.1.3.2 Single Cantilever bending tests

The single cantilever bending test is till today the most common fracture testing geometry in the small scale. Therefore, rectangular beams with a straight cut notch are used but also other beam geometries and notch shapes are reported. The cantilevers are either produced by first locally etching of the substrate material to get a free-standing film that is then further machined by FIB milling [10] or produced fully with FIB milling [41]. Finally, the notch is milled with a reduced current at the support. The cantilever is then loaded by an indenter tip until failure (see Figure 8). Fracture toughness is then calculated from fracture load, cantilever dimensions (l,b,w), crack length a and a geometric factor f(a/w), as followed by equation 3 [42]:

$$K_I = \frac{P_{max} l}{b w^{\frac{3}{2}}} f\left(\frac{a}{w}\right). \qquad (3)$$

The advantage of this geometry is, that it is easy machinable and able to test a range of materials, boundaries, and interfaces [41], but on the contrary, it is also restricted to the elastic-brittle regime. Furthermore, only the initiation fracture toughness can be obtained from such tests [41]. As can be seen in equation 3, K_I is very sensitive to the beam dimensions and the distance between the loading point and the precrack, which makes accurate measurement of the beam and in situ imaging necessary [41].

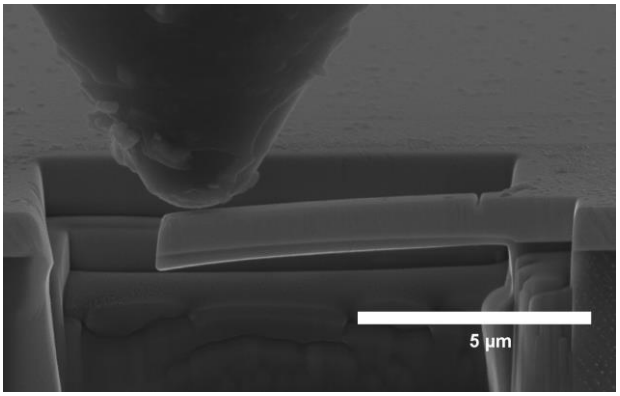

Figure 8: Single cantilever bending test.

3.1.3.3 Clamped beam bending

The configuration of this test is a modification of the classical three-point bending test with the ends clamped instead of free. The big advantage of this configuration is, that it supports stable crack growth even in brittle materials [41]. This is necessary for measuring a resistance curve or fatigue behavior of a material [43]. The main drawback of this method is the lack of analytical formulation for K_I. Consequently each test requires a finite element (FEM) simulation to extract the stress intensity factor [41].

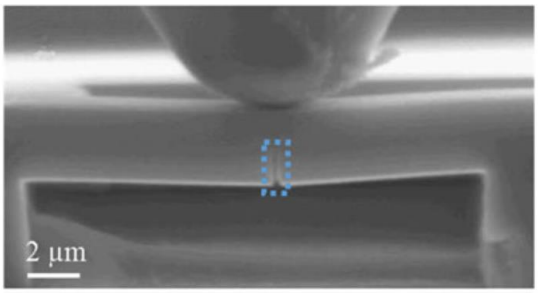

Figure 9: Clamped beam bending [41].

3.1.3.4 Pillar splitting

This method was recently developed by M. Sebastiani et al. [44] and avoids some of the shortcomings of the other methods [38]. FIB milling is used to produce cylindrical pillars that are then loaded to fracture by nanoindentation. Fracture toughness K_c is then calculated from the critical load (P_c), where the pillar fractures, the pillar radius R and a dimensionless coefficient γ based on the E/H ratio (as can be seen in equation 4).

$$K_c = \gamma \frac{P_c}{R^{1.5}} \qquad (4)$$

M. Ghidelli et al. [38] calculated γ using cohesive zone finite element modeling for different indenter angles and indentation modudulus/hardnees (E/H) ratios. The E/H ratio can be obtained from nanoindentation. FIB milled pillars should have an aspect ratio (h/D) ≥1 and a diameter that exceeds film thickness to assure surface residual stress relaxation (h is pillar height, D is top diameter of the pillar) [44].

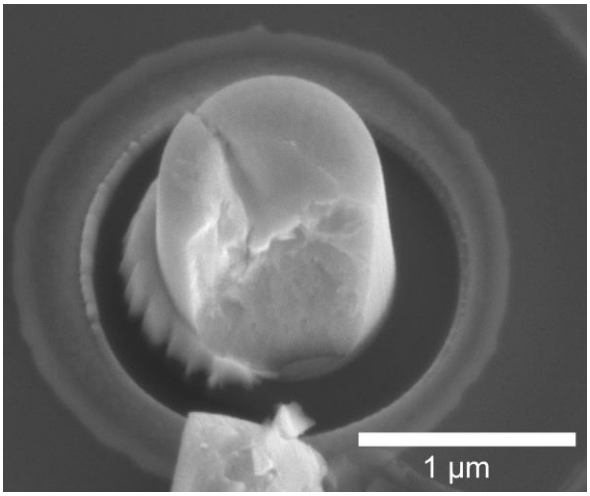

Figure 10: Pillar splitting by micro mechanical cube corner compression tests.

3.2 Ductility of ceramic coatings

Not only high hardness, but also ductility and toughness are a crucial property for thin film application of ceramic coatings. Mostly, these two material properties exclude each other. Enhancing the ductility of ceramic coatings while retaining high hardness is therefore highly desirable. Two approaches can be applied to improve ductility: 1) architectural arrangement and 2) intrinsic enhancement via adapting the bonding state.

3.2.1 Enhancement through architectural arrangement

Several approaches to enhance ductility via architectural arrangement of the film morphology are used. This includes ductile phase toughening, toughening through nanocrystalline microstructure or multilayer structure, carbon nanotube toughening, phase transformation toughening, or toughening by compressive stress (reviewed by S. Zhang et al. [45]). All these methods yield to improve the deformation energy absorption of the material and hinder a

crack to initiate or propagate. In ductile phase toughening, grains are embedded in a ductile phase, commonly a metal or an amorphous phase. Hereby, grain size and ductile phase amount influence the ductility enhancement. Multilayer arrangements often consist of stacked ductile and brittle layers, where cracks are deflected at the interfaces. Nevertheless, in most of the cases a trade-off must be made between loss of hardness and increase of ductility.

3.2.2 Intrinsic enhancement

To enhance ductility of a material intrinsically, material properties have to be changed on a more fundamental level. Whereas general statements tell that for example metals deform ductile and ceramics are brittle, fundamental knowledge on the electronic origins is still subject for investigations [46]. Nevertheless, not only electronic structure, but also the crystal structure, influences formability of for example metals. The von Mises criterion states that five independent slip systems are needed to deform a metal. Therefore, metals, which crystallize in a hexagonal structure, are more brittle than those exhibiting cubic structure. For B1 (cubic, NaCl-prototype) transition metal nitrides D. G. Sangiovanni et al. found that increasing the valence electron concentration (VEC) enhances ductility. The increased VEC furthermore enhances the occupation of the d-t_{2g} metallic states and therefore increases the metallic bonding character. They suggested that alloying Ti-Al-N with for example Mo, W or Ta improves ductility. Seidl et al. who found an increase of K_{IC} from 3.5 MPa $m^{1/2}$ for $Ti_{0.54}Al_{0.46}N$ up to 4.7 MPa $m^{1/2}$ for $Ti_{0.44}Al_{0.41}Ta_{0.15}N$.

3.3 Micromechanical testing Methods

The era of micromechanical tests started with the invention of nanoindentation and scanning probe microscopy (SPM). The introduction of micro-pillar compression tests by M. D. Uchic in 2004 [47] and the progress in the therefore required accurate sample preparation via focused ion beam milling (FIB), gave a huge boost to the field. Continuous device miniaturization down to the nanometer scale as well as mechanical characterization of nano-materials, require mechanical testing methods on the relevant length scale. Hence, these test can be relevant

also for bulk materials. According to J. R. Greer et al., micromechanical testing has pathed the way of a new era in material science, they stated: *"Rather than relying on the classical strengthening techniques utilized on bulk materials for more than a century, i.e. solution strengthening, alloying, fiber reinforcement and cold-working, the development of novel material systems with radically superior properties will be achieved through architectural control at the appropriate microstructural scales"* [16]. Therefore, gaining detailed knowledge of deformation mechanisms or other mechanical phenomena, can help to improve macroscopic material properties [48].

Since one group of micromechanical tests, with the purpose of fracture toughness determination, was already discussed in the previous chapter, the following will concentrate on the widely used micro-pillar compression tests and a comparison with nanoindentation tests.

3.3.1 Micro-pillar compression testing

Since the first demonstration by M. D. Uchic in 2004 [47], uniaxial micro compression of pillars has been developed to a widely used technique for studying small scale mechanical behavior of materials. When performing these tests, three unexpected findings for all crystalline, dislocation containing single-crystalline metals were obtained: 1) Yield strength is size dependent. Greer and Nix showed that single crystalline Au with pillar diameters below one micron have a yield strength of nearly 50 times higher than bulk [17] - 2) stochastic variation in yield stress between pillars of same size- 3) Discrete displacement bursts were observed in the load-displacement curve. This is commonly explained by the limited number and size of dislocation sources.

The experimental setup is shown in Figure 11. The pillar is compressed (load or displacement controlled) by a flat diamond punch while optical recording and monitoring applied load and displacement.

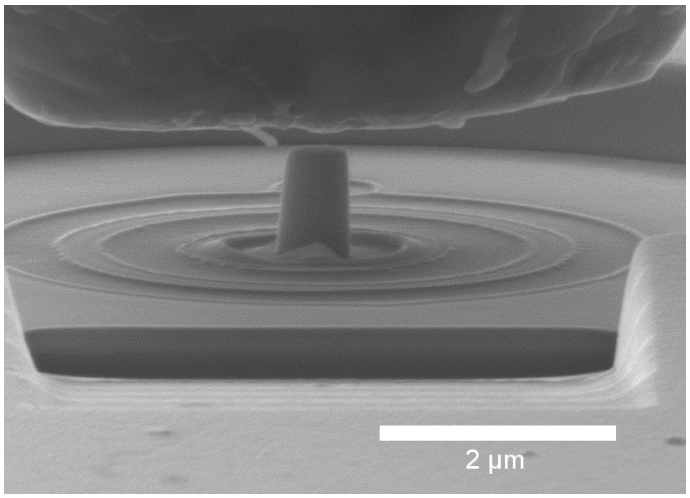

Figure 11: Micro-pillar compression test.

3.3.1.1 Sample fabrication

The most common method for producing pillars out of a deposited coating is by using a Focused Ion Beam (FIB). Therefore, two techniques – the Lathe milling and the Annular milling, are applied. Lathe milling, which was used by M. D. Uchic, yields to pillars with no taper and a good control over length and diameter. As a first step a preform ring with a larger diameter is made. Afterwards the sample is tilted relatively to the ion beam and a series of small rectangular cuts and rotating the sample removes the material from the pillars sidewall until the final geometry is reached [49].

Annular milling is used in the majority of micro-pillar compression studies. In this process, the sample stays perpendicular to the ion beam and a series of circular ring patterns with decreasing diameter and ion beam currents are performed to reach the desired dimensions of the pillar. Annular milled pillars are slightly tapered (generally within 2° to 5°) which complicates the stress-strain analysis due to the non-uniform diameter [50]. Furthermore, they exhibit slightly rounded edges. However, annular milling is much faster than Lathe milling, and additionally the pillars are exposed to a much less ion dose. J. Hütsch et al. emphasized the strong effect of the ion damage on the scaling of the stress [49].

Furthermore, other techniques are reported like producing top down square pillars with a tilt in the last step to correct the taper [51] but also techniques that do not involve an ion beam. Electrodeposition into patterned cavities, epitaxial growth of prisms, directional solidification of fibers, and lithography [52].

3.3.1.2 Experimental shortcomings and Corrections

When evaluating and interpreting the load-displacement curve obtained by the indenter and calculating engineering stress or strain, the experimental shortcomings of the micro-pillar compression tests have to be considered. First, material damage due to FIB milling can affect the material properties. This is especially relevant for small pillars. Secondly, misalignment between the pillar and indenter leads to a corrupted stress state and has to be considered when interpreting the load-displacement curve.

Strain is mainly affected by the compliance of the substrate, which can be corrected applying the Sneddon's correction. The effects of the taper on the mechanical response have been discussed in several works applying Finite Element Method (FEM) simulations [53–54]. Pillars with taper exhibit a non-uniform stress state and result in an exaggeration of work hardening parameters and increased apparent yield. Therefore, Wheeler and Michler suggest to calculate the true yield point from the smallest cross sectional area or the diameter at the top of the pillar [55].

To overcome most of these shortcomings, micro-tension tests have been introduced, with the drawback of more time consuming sample preparation (5 to 20 times longer than for pillars) [48].

3.3.1.3 Micro-pillar compression tests on thin films

One of the first works, applying micro-pillar compression tests on the investigation of mechanical properties of thin films, was done by G. Dehm et al. in 2009. They highlighted, that the method is well suited for "soft" films on "hard" substrates. Hard and brittle films showed fracture or penetration into the substrate as observed for TiN on a MgO substrate [56].

3.3.2 Nanoindentation vs. micro-pillar compression tests

The characterization of mechanical properties of thin films is very important for their design and development. The primarily used method to investigate the small-scale mechanics of thin films is Nanoindentation. This method was introduced in 1992 by Oliver and Pharr [57] for measuring hardness and elastic modulus. This is obtained from the load-displacement data during one cycle of loading and unloading from indenting the material with a diamond tip. A

common shape of the tip is the Berkovich triangular pyramid. During loading the material deforms first elastic and then plastic as the permanent hardness impression forms. During unloading it is assumed that only elastic deformation is recovered [58]. Hardness is then calculated using the maximum load P_{max} and the contact area under load A (please, see equation 5).

$$H = \frac{P_{max}}{A} \qquad (5)$$

A can be determined by the indentation depth from the loading-unloading curve in dependence of the indenter geometry. The effective Elastic modulus ($E/(1-\nu^2)$) is calculated from the contact area and unloading stiffness [56–58].

In some cases, Nanoindentation can also determine the onset of plasticity as reported by Gouldstone et al. by a sudden displacement pop-in event [59]. However, direct information of the stress-strain evolution cannot be gained from Nanoindentation. This method has been proven to be very useful, to extract Hardness and elastic modulus and is therefore widely used. Nevertheless, this method pose some drawbacks. One is the “indentation size effect”, which is manifested in increasing hardness values with decreasing indentation depth [56]. Furthermore, with increasing indentation depth, hardness values correspond to a superposition of substrate and thin film. Therefore, indentation depths should be below 10% of the film thickness [60]. Furthermore, indentation involves a complex stress/strain field underneath the indenter.

Micro-pillar compression tests have become the favored technique for in situ testing. Bulk tension and compression tests are used to study the mechanical response under uniaxial loading. The same applies for the micro-pillar compression tests, where the pillar shape yields a nearly uniaxial stress state (depending on the taper) which leads to a straightforward stress-strain analysis. Furthermore, strained volume can be directly observed [55]. Most studies applying micro-pillar compression tests focus on the onset of plasticity and plastic deformation of the material. Only a few focused on the elastic behavior, but Choi et al. showed that the method can also be applied to determine Young’s modulus for anisotropic materials [61].

List of References

1. O. Cedillos-Barraza, D. Manara, K. Boboridis, T. Watkins, S. Grasso, D. D. Jayaseelan, R. J. M. Konings, M. J. Reece, & W. E. Lee, Investigating the highest melting temperature materials: A laser melting study of the TaC-HfC system. *Scientific Reports*, **6** (2016) 37962. https://doi.org/10.1038/srep37962.
2. W. S. Williams, TRANSITION-METAL CARBIDES. (1971).
3. D. J. Rowcliffe & G. E. Hollox, Plastic flow and fracture of tantalum carbide and hafnium carbide at low temperatures. *Journal of Materials Science*, **6** (1971) 1261–1269. https://doi.org/10.1007/BF00552039.
4. R. Westergård, M. Bromark, M. Larsson, P. Hedenqvist, & S. Hogmark, Mechanical and tribological characterization of DC magnetron sputtered tantalum nitride thin films. *Surface and Coatings Technology*, **97** (1997) 779–784. https://doi.org/10.1016/S0257-8972(97)00338-1.
5. C.-S. Shin, D. Gall, P. Desjardins, A. Vailionis, H. Kim, I. Petrov, J. E. Greene, & M. Odén, Growth and physical properties of epitaxial metastable cubic TaN(001). *Applied Physics Letters*, **75** (1999) 3808–3810. https://doi.org/10.1063/1.125463.
6. N. Koutná, D. Holec, M. Friák, P. H. Mayrhofer, & M. Šob, Stability and elasticity of metastable solid solutions and superlattices in the MoN-TaN system: a first-principles study. (2017) 1–12.
7. Y. Y. Guu & J. F. Lin, Comparison of the tribological characteristics of titanium nitride and titanium carbonitride coating films. *Surface & Coatings Technology*, **85** (1996) 146–155.
8. Q.-J. Hong & A. van de Walle, Prediction of the material with highest known melting point from ab initio molecular dynamics calculations. *Physical Review B*, **92** (2015) 20104. https://doi.org/10.1103/PhysRevB.92.020104.
9. R. Bermejo, R. Daniel, C. Schuecker, O. Paris, R. Danzer, & C. Mitterer, Hierarchical Architectures to Enhance Structural and Functional Properties of Brittle Materials. *Advanced Engineering Materials*, **19** (2017). https://doi.org/10.1002/adem.201600683.
10. R. Hahn, M. Bartosik, R. Soler, C. Kirchlechner, G. Dehm, & P. H. Mayrhofer, Superlattice

effect for enhanced fracture toughness of hard coatings. *Scripta Materialia*, **124** (2016) 67–70. https://doi.org/10.1016/j.scriptamat.2016.06.030.

11. V. Moraes, H. Riedl, C. Fuger, H. Bolvardi, P. Polcik, D. Holec, & P. H. Mayrhofer, Ab-initio inspired design of ternary boride thin films. *submitted to Scientific Reports*, (2018).
12. S. Kiani, C. Ratsch, A. M. Minor, J. M. Yang, & S. Kodambaka, In situ transmission electron microscopy observations of room-temperature plasticity in sub-micron-size TaC(100) and TaC(011) single crystals. *Scripta Materialia*, **100** (2015) 13–16. https://doi.org/10.1016/j.scriptamat.2014.11.036.
13. M. D. Uchic, D. M. Dimiduk, J. N. Florando, & W. D. Nix, Sample dimensions influence strength and crystal plasticity. *Science (New York, N.Y.)*, **305** (2004) 986–9. https://doi.org/10.1126/science.1098993.
14. S. Liu, R. Raghavan, X. T. Zeng, J. Michler, W. J. Clegg, S. Liu, R. Raghavan, X. T. Zeng, J. Michler, & W. J. Clegg, Compressive deformation and failure of CrAlN/Si3N4 nanocomposite coatings. *Applied Physics Letters*, **104** (2014) 81919. https://doi.org/https://doi.org/10.1063/1.4867017.
15. D. Kiener, C. Motz, & G. Dehm, Micro-compression testing : A critical discussion of experimental constraints. **505** (2009) 79–87. https://doi.org/10.1016/j.msea.2009.01.005.
16. J. R. Greer, J. Th, & M. De Hosson, Plasticity in small-sized metallic systems: Intrinsic versus extrinsic size effect. *Progress in Materials Science*, **56** (2011) 654–724. https://doi.org/10.1016/j.pmatsci.2011.01.005.
17. J. R. Greer & W. D. Nix, Size dependence of mechanical properties of gold at the sub-micron scale. *Applied Physics A: Materials Science and Processing*, **80** (2005) 1625–1629. https://doi.org/10.1007/s00339-005-3204-6.
18. M. Grumski, P. P. Dholabhai, & J. B. Adams, Ab initio study of the stable phases of 1:1 tantalum nitride. *Acta Materialia*, **61** (2013) 3799–3807. https://doi.org/10.1016/j.actamat.2013.03.018.
19. K. Frisk, Analysis of the phase diagram and thermochemistry in the Ta–N and the Ta–C–N systems. *Journal of Alloys and Compounds*, **278** (1998) 216–226. https://doi.org/10.1016/S0925-8388(98)00582-9.
20. H. Riedl, T. Glechner, T. Wojcik, N. Koutná, S. Kolozsvári, V. Paneta, D. Holec, D. Primetzhofer, & P. H. Mayrhofer, Influence of carbon deficiency on phase formation

and thermal stability of super-hard TaC y thin films. *Scripta Materialia*, **149** (2018) 150–154. https://doi.org/10.1016/j.scriptamat.2018.02.030.

21. P. Violet, E. Blanquet, & O. Le Bacq, Density functional study of the stability and electronic properties of TaxNy compounds used as copper diffusion barriers. *Microelectronic Engineering*, **83** (2006) 2077–2081. https://doi.org/10.1016/j.mee.2006.09.011.
22. S. Du, K. Zhang, Q. Meng, P. Ren, C. Hu, M. Wen, & W. Zheng, N dependent tribochemistry: Achieving superhard wear-resistant low-friction TaCxNyfilms. *Surface and Coatings Technology*, **328** (2017) 378–389. https://doi.org/10.1016/j.surfcoat.2017.09.006.
23. W. G. Fahrenholtz, E. J. Wuchina, W. E. Lee, & Y. Zhou, *Ultra-High Temperature Ceramics Materials for Extreme Environment Applications* (2014).
24. H. O. Pierson, *Handbook of refractory carbides and nitrides : properties, characteristics, processing, and applications* (Noyes Publications, 1996).
25. L. Toth, *Transition Metal Carbides and Nitrides.* (Elsevier Science, 1971).
26. E. Parthé, K. Yvon, & IUCr, On the crystal chemistry of the close packed transition metal carbides. II. A proposal for the notation of the different crystal structures. *Acta Crystallographica Section B Structural Crystallography and Crystal Chemistry*, **26** (1970) 153–163. https://doi.org/10.1107/S0567740870002108.
27. F. Kubel, W. Lengauer, K. Yvon, K. Knorr, & A. Junod, Structural phase transition at 205 K in stoichiometric vanadium nitride. *Physical Review B*, **38** (1988) 12908–12912. https://doi.org/10.1103/PhysRevB.38.12908.
28. P. Rogl & M. Materials Science International Team, The C-Ta phase diagram: Datasheet from MSI Eureka in SpringerMaterials (https://materials.springer.com/msi/phase-diagram/docs/sm_msi_r_10_011533_02_full_LnkDia0). (n.d.).
29. Powder diffraction file 00-035-0801, International Center for Diffraction Data. *PDF-4+*, (2015).
30. Powder diffraction file 00-049-1283, International Center for Diffraction Data. *PDF-4+*, (2015).
31. W. Lengauer, Transition Metal Carbides, Nitrides, and Carbonitrides. *Handb. Ceram. Hard Mater.* (Weinheim, Germany: Wiley-VCH Verlag GmbH), pp. 202–252. https://doi.org/10.1002/9783527618217.ch7.

32. C. K. Jun & P. T. B. Shaffer, Elastic moduli of niobium carbide and tantalum carbide at high temperature. *Journal of the Less Common Metals*, **23** (1971) 367–373. https://doi.org/10.1016/0022-5088(71)90046-4.

33. J. Robertson, Diamond-like amorphous carbon. *Materials Science and Engineering: R: Reports*, **37** (2002) 129–281. https://doi.org/10.1016/S0927-796X(02)00005-0.

34. U. Jansson & E. Lewin, Sputter deposition of transition-metal carbide films - A critical review from a chemical perspective. *Thin Solid Films*, **536** (2013) 1–24. https://doi.org/10.1016/j.tsf.2013.02.019.

35. S. Jhi, J. Ihm, & S. G. Louie, Electronic mechanism of hardness enhancement in transition-metal carbonitrides. **399** (1999) 1–3.

36. X. K. Zhu & J. A. Joyce, Review of fracture toughness (G, K, J, CTOD, CTOA) testing and standardization. *Engineering Fracture Mechanics*, **85** (2012) 1–46. https://doi.org/10.1016/j.engfracmech.2012.02.001.

37. T. Anderson, *Fracture mechanics: fundamentals and applications*, fourth edi (2017).

38. M. Ghidelli, M. Sebastiani, K. E. Johanns, & G. M. Pharr, Effects of indenter angle on micro-scale fracture toughness measurement by pillar splitting. *Journal of the American Ceramic Society*, **100** (2017) 5731–5738. https://doi.org/10.1111/jace.15093.

39. J. P. Best, J. Zechner, J. M. Wheeler, R. Schoeppner, M. Morstein, & J. Michler, Small-scale fracture toughness of ceramic thin films: the effects of specimen geometry, ion beam notching and high temperature on chromium nitride toughness evaluation. *Philosophical Magazine*, **96** (2016) 3552–3569. https://doi.org/10.1080/14786435.2016.1223891.

40. K. E. Johanns, J. H. Lee, Y. F. Gao, & G. M. Pharr, An evaluation of the advantages and limitations in simulating indentation cracking with cohesive zone finite elements. *Modelling and Simulation in Materials Science and Engineering*, **22** (2014). https://doi.org/10.1088/0965-0393/22/1/015011.

41. B. N. Jaya, C. Kirchlechner, & G. Dehm, Can microscale fracture tests provide reliable fracture toughness values? A case study in silicon. *Journal of Materials Research*, **30** (2015) 686–698. https://doi.org/10.1557/jmr.2015.2.

42. K. Matoy, H. Schönherr, T. Detzel, T. Schöberl, R. Pippan, C. Motz, & G. Dehm, A comparative micro-cantilever study of the mechanical behavior of silicon based passivation films. *Thin Solid Films*, **518** (2009) 247–256.

https://doi.org/10.1016/j.tsf.2009.07.143.

43. H. Li & J. J. Vlassak, Determining the elastic modulus and hardness of an ultra-thin film on a substrate using nanoindentation. *Journal of Materials Research*, **24** (2009) 1114–1126. https://doi.org/10.1557/jmr.2009.0144.

44. M. Sebastiani, K. E. Johanns, E. G. Herbert, F. Carassiti, & G. M. Pharr, A novel pillar indentation splitting test for measuring fracture toughness of thin ceramic coatings. *Philosophical Magazine*, **95** (2015) 1928–1944. https://doi.org/10.1080/14786435.2014.913110.

45. S. Zhang, D. Sun, Y. Fu, & H. Du, Toughening of hard nanostructural thin films: A critical review. *Surface and Coatings Technology*, **198** (2005) 2–8. https://doi.org/10.1016/j.surfcoat.2004.10.020.

46. D. G. Sangiovanni, V. Chirita, & L. Hultman, Toughness enhancement in TiAlN-based quarternary alloys. *Thin Solid Films*, **520** (2012) 4080–4088. https://doi.org/10.1016/j.tsf.2012.01.030.

47. M. D. Uchic, Sample Dimensions Influence Strength and Crystal Plasticity. *Science*, **305** (2004) 986–989. https://doi.org/10.1126/science.1098993.

48. G. Dehm, B. N. Jaya, R. Raghavan, & C. Kirchlechner, Overview on micro- and nanomechanical testing: New insights in interface plasticity and fracture at small length scales. *Acta Materialia*, **142** (2018) 248–282. https://doi.org/10.1016/j.actamat.2017.06.019.

49. J. Hütsch & E. T. Lilleodden, The influence of focused-ion beam preparation technique on microcompression investigations: Lathe vs. annular milling. *Scripta Materialia*, **77** (2014) 49–51. https://doi.org/10.1016/j.scriptamat.2014.01.016.

50. M. D. Uchic, P. A. Shade, & D. M. Dimiduk, Plasticity of Micrometer-Scale Single Crystals in Compression. *Annual Review of Materials Research*, **39** (2009) 361–386. https://doi.org/10.1146/annurev-matsci-082908-145422.

51. M. Schamel, J. M. Wheeler, C. Niederberger, J. Michler, A. Sologubenko, & R. Spolenak, Cyclic loading for the characterisation of strain hardening during in situ microcompression experiments. *Philosophical Magazine*, **96** (2016) 3479–3501. https://doi.org/10.1080/14786435.2016.1235290.

52. W. Kang, M. Merrill, & J. M. Wheeler, In situ thermomechanical testing methods for micro/nano-scale materials. *Nanoscale*, **9** (2017) 2666–2688.

https://doi.org/10.1039/C6NR07330A.

53. A. Abraham, Evaluation of Micro-Pillar Compression Tests for Accurate Determination of Elastic-Plastic Constitutive Relations. *Journal of Applied Mechanics*, **79** (2012) 61011. https://doi.org/10.1115/1.4006767.

54. H. Zhang, B. E. Schuster, Q. Wei, & K. T. Ramesh, The design of accurate micro-compression experiments. *Scripta Materialia*, **54** (2006) 181–186. https://doi.org/10.1016/j.scriptamat.2005.06.043.

55. J. M. Wheeler & J. Michler, Elevated temperature, nano-mechanical testing in situ in the scanning electron microscope. *Review of Scientific Instruments*, **84** (2013) 45103. https://doi.org/10.1063/1.4795829.

56. G. Dehm, H. P. Wörgötter, S. Cazottes, J. M. Purswani, D. Gall, C. Mitterer, & D. Kiener, Can micro-compression testing provide stress – strain data for thin fi lms ? A comparative study using Cu , VN , TiN and W coatings. *Thin Solid Films*, **518** (2009) 1517–1521. https://doi.org/10.1016/j.tsf.2009.09.070.

57. W. C. Oliver & G. M. Pharr, An improved technique for determining hardness and elastic modulus using load and displacement sensing indentation experiments. *Journal of Materials Research*, **7** (1992) 1564–1583. https://doi.org/10.1557/JMR.1992.1564.

58. W. C. Oliver & G. M. Pharr, Measurement of hardness and elastic modulus by instrumented indentation: Advances in understanding and refinements to methodology. *Journal of Materials Research*, **19** (2004) 3–20. https://doi.org/10.1557/jmr.2004.19.1.3.

59. A. Gouldstone, N. Chollacoop, M. Dao, J. Li, A. M. Minor, & Y. L. Shen, Indentation across size scales and disciplines: Recent developments in experimentation and modeling. *Acta Materialia*, **55** (2007) 4015–4039. https://doi.org/10.1016/j.actamat.2006.08.044.

60. R. Saha & W. D. Nix, Effects of the substrate on the determination of thin mechanical properties by nanoindentation. *Acta Materialia*, **50** (2002) 23–28. https://doi.org/10.1016/S1359-6454(01)00328-7.

61. I. Choi, Y. Gan, D. Kaufmann, O. Kraft, & R. Schwaiger, Measurement of Young's modulus of anisotropic materials using microcompression testing. *Journal of Materials Research*, **27** (2012) 2752–2759. https://doi.org/10.1557/jmr.2012.18.

4 Publications

Publication I

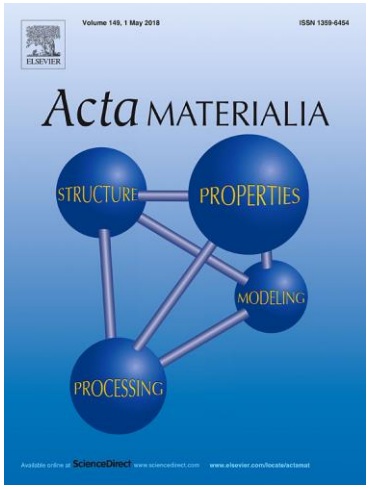

Tuning thermo-mechanical properties of Ta-C-N coatings by non-metallic alloying – A combinatorial approach

T. Glechner, S. Kolozsvári, S. Fritze, E. Lewin,
V. Paneta, D. Primetzhofer, D. Holec, P.H. Mayrhofer, and H. Riedl

(April 2018, manuscript in final preparation)

Tuning thermo-mechanical properties of Ta-C-N coatings by non-metallic alloying – A combinatorial approach

T. Glechner[a], S. Kolozsvári[b], S. Fritze[c], E. Lewin[c],

V. Paneta[d], D. Primetzhofer[d], D. Holec[e], P.H. Mayrhofer[a], and H. Riedl[a]

[a] Institute of Materials Science and Technology, TU Wien, A-1060 Wien, Austria

[b] Plansee Composite Materials GmbH, D-86983 Lechbruck am See, Germany

[c] Department of Chemistry - Ångström Laboratory, Uppsala University, SE-75120 Uppsala, Sweden

[d] Department of Physics and Astronomy, Uppsala University, SE-75120 Uppsala, Sweden

[e] Department of Physical Metallurgy and Materials Testing, Montanuniversität Leoben, A-8700 Leoben, Austria

Tailoring thermomechanical properties of transition metal carbides by substituting carbon with nitrogen atoms is a highly interesting approach, changing the bonding state towards a more metallic like character through non-metals – hence increasing ductility. Based on ab initio calculations we could experimentally proof, that up to a nitrogen content of about 65 % on the non-metallic sublattice, Ta-C-N crystals prevail a face centered cubic structure in sputter deposited thin films. The cubic structures are partly stabilized by both non-metal and Ta vacancies, whereas metal defects are decisive for nitrogen rich compositions. With increasing nitrogen super-hard fcc-$TaC_{0.71}$ thin films weakens from around 40 GPa to 25 GPa for $TaC_{0.32}N_{0.68}$, respectively, accompanied by a linear decrease in indentation modulus. Through the substitution of C with N a thermally driven decomposition of the coatings can be retarded for around 200 °C. This study emphasizes an alternative alloying concept for ceramic thin film materials, by forming solid solutions on the non-metallic sublattice, designing intrinsic coating properties.

Keywords: TaCN; Thin films; Vacancies; UHTC; Density Functional Theory (DFT); Carbonitrides;

***Corresponding author's e-mail address:** thomas.glechner@tuwien.ac.at

Introduction

Transition metal (TM) carbides and nitrides belong to the class of ultra-high temperature ceramics (UHTC) exhibiting highly interesting properties such as extreme hardness, highest thermal and chemical stability, or excellent thermal conductivity. Therefore, these TM ceramics are well established in various industrial applications, especially in form of thin films. Here the field of protective coatings but also microelectronics (e.g. diffusion barriers or piezo-electric applications) gained a lot of scientific and industrial attention for nitride-based systems containing Ti and/or Al [1]. Among TM carbides Ta-C has the highest melting temperature of all known binary systems (3983 °C [2]) and in relation to the predominant covalent-metallic bonding character extreme hardness and chemical inertness [3]. However, for a broad utilization of Ta-C based materials – either as structural components or thin films – the tremendously low ductility and extremely high fracture appearance transition temperature (about $0.5 \cdot T_m$) are major limiting issues. In general, improving the ductility of TM carbides (as well as nitrides) while retaining other thermo-mechanical properties is highly desired for a variety of applications. Basic mechanisms to increase the ductility of ceramic materials are the incorporation of ductile phases, grain boundary engineering, or varying crystallite and grain sizes. For thin film materials, architectural arrangements such as superlattices or hierarchical composites achieved interesting results concerning fracture toughness enhancements [4–5] – K_{IC} increases by one order of magnitude. However, for an intrinsic increase of the ductility, thin film materials design needs to be conducted on the atomic scale range adapting the bonding character [6]. One highly attractive method to adjust the properties of Ta-C (on an atomistic level) is a partly substitution of carbon by nitrogen on the non-metallic sublattice. This approach can be seen as a solid-solution of non-metallic atoms on their sublattice. In contrast to various TM carbides (e.g. TaC_y, HfC_y, ZrC_y), which are stabilized in the face centered cubic (fcc) NaCl ($Fm\bar{3}m$, #225) structure, crystalizes TaN predominantly in hexagonal (hex) structure types. Two highly similar prototypes, ε-TaN (P6/mmm, #191) and π-TaN ($P\bar{6}2m$, #189) are known for Ta-N, whereas π-TaN is reported to be the most stable one [7]. However in the equilibrium state a transition from π-TaN to fcc structured δ-TaN ($Fm\bar{3}m$, #225) is observed at 1950 °C – (according to [8]) highlighting the possibility of accessing pure fcc solid solutions. Nevertheless, both systems are well known for phase stabilizing effects through defects, e.g. vacancies or Schottky defects. For TaC_y the

influence of carbon deficiencies is more decisive as for Ta_yN, where metallic vacancies are crucial [3–9]. In general, the relation to vacancy stabilized structures leads to a well-known anomalous hardness increase at VEC of about 8.4 e/f.u. for TMCs (individual non-stoichiometric compositions for each system [10]). Furthermore, a recent study [9] also emphasized a ductile behavior of partly vacancy stabilized Ta-N applying density functional theory (DFT) calculations. Physical vapor deposition (PVD) is known to enable the accesses of meta-stable phases due to highly limited ad-atom kinetics during film growth (extremely high cooling rates 10^{13} K s^{-1}) and a pronounced introduction of structural defects, such as point defects. Considering all these aspects, a stabilization of fcc structured Ta-C-N by PVD is highly presumable [11]. To date, TaC_xN_{1-x} thin films have only been subjected as diffusion barriers between copper and silicon in semiconductor devices, but their mechanical properties, especially in a highly crystalline constitution, are relatively unexplored [11–12].

In this work, we use a computational guided approach to fundamentally explore phase stabilizing effects of vacancies in relation to the C/(C+N) ratio and their related mechanical properties. Furthermore, decomposition kinetics of TaC_xN_{1-x} coatings are correlated with their structure-property relationships after various thermal treatments.

Experimental Procedures

Ta-C and Ta-C-N thin films were deposited using an UHV magnetron sputtering system (AJA Orion 5), utilizing a 3-inch $TaC_{0.97}$ compound as well as two 2-inch Ta targets (Plansee Composite Materials GmbH [13]). All Ta-C films were sputtered in pure Ar atmosphere (purity 99.999%) whereas Ta-C-N and Ta-N films were deposited in Ar and N gas mixtures. The Ta-C target was operated in pulsed mode (pulse frequency 150 kHz with a pulse width of 2576 ns), whereas the Ta targets were driven under DC current. All depositions were carried out at a working gas pressure of 0.4 Pa with a total gas flow rate of 20 sccm. By varying the nitrogen to total flow rate, the amount of N within the Ta-C-N coating was adapted – $f_{[N_2]}^{norm} = \frac{f_{[N_2]}}{f_{[N_2]}+f_{[Ar]}}$ varied between 0.05 to 0.5 – for further details see Table 1. During the depositions, the heater temperature was set to 600 °C, which corresponds to a substrate temperature of about 425±10 °C, combined with a bias voltage of -10 V. Prior to the deposition processes, all targets and substrates were sputter-cleaned in pure Ar atmospheres (total pressure of 6.0 Pa). All coatings were deposited on polished single crystalline Si strips (100 oriented, 20x7x0.38 mm^3),

as well as polished single crystalline Al_2O_3 platelets (1-102 oriented, 10x10x0.5 mm^3). Furthermore, selected compositions were additionally carried out on 0.05 mm thin steel foils, which were subsequently dissolved in nitric acid, to obtain powdered coating materials. These powders were used for X-ray diffraction (XRD) as well as annealing treatments to ensure interference free analysis.

Structural investigations of all coatings (either on hard substrates as well as in powdered state) were done by X-Ray diffraction in Bragg Brentano configuration applying a Panalytical Empyrean diffractometer equipped with a Cu-K_α radiation source (wave length λ = 1.54 Å). The chemical composition of all thin films was investigated by Time-of-Flight Elastic Recoil Detection Analysis (TOF-ERDA) [14] with a 36 MeV I^{8+} primary ion beam under a recoil detection angle of 45 °. Avoiding surface contaminations, the chemical compositions were evaluated for depths below at least 30 nm. The expected systematic uncertainties for the light elements (C and N) in the Ta-C-N system are found to be at most 5 to 10 % of the detected concentrations for absolute measurements free from standards. This error is mainly due to uncertainties in the specific energy loss of the recoiling particles. The authors want to note, that much higher accuracy is obtained for inter-sample comparison, as it is done within this study. Specific sources and consequences of systematic uncertainties are discussed in more detail by Zhang et al. [15]. In addition, to access the chemical bonding states within the films, we utilized X-ray photoelectron spectroscopy (XPS) – using a Physical Electronics Quantera II with monochromatic Al K_α radiation and a take-off angle of 45° for the photoelectrons. High-resolution spectra were acquired after sputter-etching (45 min with 200 eV Ar^+ ions) the films on Si (100)-substrates. The analysis area was 100 µm in diameter and the sputter-etched area about 1 x 1 mm^2. The coating morphology as well as structural evolution – especially with respect to nitrogen content – was investigated by electron microscopy utilizing scanning electron microscopy (SEM, FEI Quanta 250 FEGSEM operated at 5 keV) as well as transmission electron microscope (TEM FEI TECNAI G20, acceleration voltage of 200 kV), respectively.

The kinetic decomposition behavior of selected coatings was investigated by a combined differential scanning calorimetry (DSC)/-thermo-gravimetric analysis (TGA) system, which was equipped with a Rhodium oven (Netzsch STA 449 F1). For these analyses, powdered coating materials were weighted into platinum crucibles and subsequently heated up to 1580 °C in an inert atmosphere (He) – heating rate of 10 K/min was applied. After reaching the desired temperatures, the system was cooled down passively, achieving about 50 K/min till 500 °C.

Prior to this procedure, all samples were thermally cleaned (for 20 min) within the DSC/TG system at 150 °C. In addition, annealing treatments on sapphire substrates were performed in a vacuum annealing furnace (Centorr Vacuum Industries Series LF) up to 1400 °C. Here, we utilized heating rates of 20 K/min with dwells of 10 min at the desired temperatures.

Indentation modulus, E, and Hardness, H, were obtained by nanoindentation experiments carried out on Si as well as sapphire substrates utilizing an UMIS-equipped with a Berkovich diamond tip. At least 25 load displacement curves (per sample) were recorded at different loads (varying between 45 to 3 mN), which were analyzed after Oliver and Pharr [16]. Residual stresses within the thin films were analyzed out of the curvature utilizing the modified Stoney equation [17] – carried out on coated Si substrates. The curvature was measured by an optical profilometry (Nanovea PS50).

Calculational Methodology

Investigating the transition between fcc or hexagonal structured TaC_xN_{1-x}, we utilized Density Functional Theory (DFT) calculations implemented within the VASP (Vienna ab initio simulation package) code [18–19] using the projector augmented plane wave (PAW) pseudopotentials. To gain a deeper insight on the variations within the used pseudopotentials, we compared two different exchange correlation potential approximations, Local Density Approximation (LDA) as well as the Generalized Gradient Approximation (GGA) [20] with a Perdew-Burke-Ernzerhof (PBE) exchange correlation functional [21]. We used the following crystallographic prototypes: fcc, $Fm\bar{3}m$, #SG 225, and hex, $P\bar{6}2m$, #SG 189 – as well-known structures for the binaries. From the conventional 8-atomic (cubic) and 6-atomic (hexagonal) unit cells, 2x2x2 and 2x2x3 supercells with 64 and 72 atoms, respectively, were created to model various TaC_xN_{1-x} compositions. The compositional variation was obtained by substituting carbon atoms with nitrogen utilizing the Special Quasi-random Structure (SQS) method [22]. The influence of structural defects was investigated by a systematic remove of either metal or non-metallic atoms, also applying SQS. To gain highest accuracy with respect to proper computational time, a plane wave cut-off energy of 600 eV with a k-mesh obtaining 50 subdivisions in each direction within the Brillouin zone was chosen. Equilibrium lattice parameters and minimum energy were obtained by relaxing the supercell volumes, shapes and atomic positions (ISIF 3 Tag in VASP). To also obtain elastic constants of the TaC_xN_{1-x} system the Universal Linear-Independent Coupling Strain (ULICS) method [23] was utilized.

Results and Discussion

In order to theoretically explore the influence of either nitrogen or carbon on the corresponding stable binary structures – fcc-TaC_y and hex-TaN, respectively – we varied the non-metal sublattice occupation x of our TaC_xN_{1-x} structures in increments of x = 0.25 within the DFT based calculations. In Figure 1a the energy of formation, E_f, for perfect and Ta deficient structures (two atoms removed on the sublattice – vacancy content 6%) is presented – full symbols with solid lines denote to the perfect crystals, whereas half-filled with dash-dotted lines to Ta vacant ones. In the whole manuscript, blue squares refer to fcc crystals as well as orange hexagons to the hexagonal structure type, respectively. E_f was calculated using equation 1, where $\mathrm{E}_0^{\mathrm{per/def}}$ denotes the total energy of the relaxed supercell divided by the total number of atoms in the cell. E_i is the total energy of each element in its bulk state per atom (bcc Ta, graphite C, and N) and hence n_i is the number of atoms of each species.

$$E_f = E_0^{per/def} - \frac{1}{\sum_i n_i} \cdot \sum n_i E_i \qquad (1)$$

In general, for the perfect and Ta-vacant cells, E_f decreases with increasing amount of nitrogen, highlighting the transition between fcc and hex TaC_xN_{1-x} in the range of x = 0.42. In accordance to former DFT studies [24], we also observe a stabilization of fcc-TaN and highly nitrogen rich fcc-TaC_xN_{1-x} by Ta vacancies, as likewise suggested by Koutna et al. (mentioned most stable configuration $Ta_{0.78}N$). Here the authors want to mention, that the E_f difference between the perfect and non-metal vacant cells is minor, and will be treated in more detail. Hence, to gain a more surveying insight on the stabilizing effects of the different vacancy species (especially non-metallic ones) the energy of formation of vacancies, $\mathrm{E}_\mathrm{f}^{\mathrm{vac}}$ calculated after [13], is presented in Figure 1 b, where we distinguish in principle between vacancies on the metal sublattice (Ta vacancies) and on the non-metal sublattice (C and N vacancies randomly distributed, vacancy concentration of 6%), respectively. Here we clearly see, that for the fcc-structured cells the non-metal vacancies are energetically less expensive compared to Ta vacancies, whereas at very high nitrogen contents (above x = 0.20) both types are presumable, as the $\mathrm{E}_\mathrm{f}^{\mathrm{vac}}$ turns into the negative region. For the hexagonal structure type, we only calculated $\mathrm{E}_\mathrm{f}^{\mathrm{vac}}$ up to x = 0.5 starting on the nitrogen rich side, as for all vacancy types $\mathrm{E}_\mathrm{f}^{\mathrm{vac}}$ is energetically less preferable as compared to the fcc cells. Due to the very low $\mathrm{E}_\mathrm{f}^{\mathrm{vac}}$ of non-metal vacancies, meaning in the keen positive range of 215 meV to 951 meV, a

stabilization of TaC_xN_{1-x} by either nitrogen or carbon vacancies is quite likely. In addition, to separate the effect of especially N and C, but also Ta vacancies on TaC_xN_{1-x}, we also performed selected calculations only removing carbon, nitrogen, or tantalum atoms, respectively. For just one vacancy of N, C, or Ta for x = 0.50 and 0.25 in TaC_xN_{1-x}, respectively, we reveal the following ordering: $E_f^{N_{vac}} > E_f^{Ta_{vac}} > E_f^{C_{vac}}$ for $TaC_{0.50}N_{0.50}$ which changes to $E_f^{N_{vac}} > E_f^{C_{vac}} > E_f^{Ta_{vac}}$ for $TaC_{0.25}N_{0.75}$. This highly interesting effect is in principle in line with the former results, that for nitrogen rich compositions Ta vacancies are decisive, but here the authors also want to mention, that through local ordering effects, maybe this strongly deviating result compared to the E_f^{vac} presented in Figure 1 b is related to the number of removed atoms. However, to also obtain a more assailable parameter for comparison to experiments we evaluated the evolution of the lattice constant for fcc-structured TaC_xN_{1-x}. In Figure 1c the lattice parameter for perfect as well as metal and non-metal vacant cells (vacancy concentration of 6% for Ta and C/N) are presented. Through the introduction of nitrogen replacing carbon, the lattice parameter decreases from around 4.48 to 4.43 Å for fcc-TaC to fcc-TaN. This is in principle in agreement with the atomic radii of r_C = 70 pm and r_N = 65 pm, respectively [25]. The introduction of either Ta or C/N vacancies even decreases it a little bit more, about 0.02 Å over the full range. These results also allows us to monitor the accuracy of the DFT calculations comparing the calculated lattice constants of TaC and TaN with experimentally observed values. Except missing details on the off-stoichiometry of the investigated compositions in literature data, TaC exhibits a lattice constant of 4.45 Å (PDF 4+, 00-035-0801) in relation to 4.42 Å and 4.48 Å obtained with LDA and PBE potentials, respectively. Especially, for TaC_y our former study [3] highlighted, that DFT overestimates the lattice constant as well as that TaC_y is compositionally stabilized in the range of $TaC_{0.76}$ (annealed at ≥ $0.5 \cdot T_m$) with a lattice constant of 4.42 Å [3]. For metastable cubic δ-TaN the reported experimental lattice constants vary from 4.33 Å (PDF 4+, 00-049-1283) to 4.42 Å (PDF 2, 03-065-9404) beeing also in good agreement with lattice constants received using LDA (4.36 Å) and PBE (4.42 Å). To highlight also the influence of the different potentials on the DFT results (and hence lattice constants) we plotted the obtained phase transitions between fcc and hex structures for LDA and PBE potentials, as well as the influence of structural defects in Figure 2. Due to the use of different potentials the intersection of the E_f curves of cubic and hexagonal structure moves from x = 0.28 for PBE (solid lines) to x = 0.22 for LDA (dashed lines), respectively. In addition, the introduction of both non-metal and metal vacancies shifts the phase transition between the

competing structures from x = 0.42 for perfect crystals (gray shaded striped area) to x = 0.22 for the Ta vacant cells (magenta cross-striped area). These areas do not represent a two-phase field in relation to the ternary phase diagram, but more an error bar of the real intersection. These colored regions are also given in the ternary system Ta-C-N, where all experimental compositions are indicated with respect to their structure and chemistry, see Figure 4. In summary, the DFT results pointed out that vacancies – non-metallic and Ta ones – enable a solid solution of cubic Ta-C and Ta-N at higher nitrogen contents.

In Figure 3a the relation between the used N partial pressure and preserved chemical compositions is presented. Already a nitrogen partial pressure of only $f_{[N_2]}^{norm}$ = 0.05 lead to a substitution of about 25 % carbon atoms on the non-metallic sublattice, with a corresponding chemical composition of $Ta_{0.51}C_{0.37}N_{0.12}$. This clear trend is obvious till $f_{[N_2]}^{norm}$ = 0.15, replacing around half of the carbon atoms by nitrogen, $Ta_{0.48}C_{0.27}N_{0.25}$. At even higher nitrogen partial pressures, e.g. $f_{[N_2]}^{norm}$ = 0.3 or 0.5 (see details in Table 1), the authors want to highlight that the overall metal to non-metal ratio decreases from around 1 to values between 0.75 or even 0.61. This is a strong indication for vacancy stabilized non-stoichiometric crystals, and needs to be correlated with structural data. Especially, the normalized notation of TaC_xN_{1-x} would be then misleading, deviating from the 'solid-solution' model on the non-metallic sublattice. Therefore, the corresponding structural data of the points presented in Figure 3a are plotted in 3b, indicated by the absolute chemical compositions. However, pure $TaC_{0.71}$ obtains mainly a fcc structure, whereby the small shoulder of the 220 peak can maybe assigned to very minor amounts of Ta_2C phase (PDF 4+, 04-010-9382). In contrast, all TaC_xN_{1-x} compositions are single phase fcc structured. The increasing nitrogen flow rate in the deposition process and hence chemical composition, also nicely shifts the indicated peaks from fcc-TaC to fcc-TaN. As abovementioned, up to a nitrogen partial pressure of $f_{[N_2]}^{norm}$ = 0.15 the metal to non-metal ratio stays around 1, which seems also to be an indication for fcc single phased structured coatings. The coating with the composition of $Ta_{0.38}C_{0.20}N_{0.42}$, deposited at $f_{[N_2]}^{norm}$ = 0.5, still appears as a fcc structure, whereby the broad peak shape and even stronger shift to fcc-TaN indicates not a pure single phased crystal. However, both aspects highlight also the influence of Ta vacancies stabilizing still a face-centered cubic crystal. For pure $TaN_{1.08}$ a dual phased structure between predominant fcc-TaN as well as hex-TaN is assumed. In addition, the off-stoichiometry and hence stabilization by Ta vacancies is obvious. The estimated integral

breadth of the 111 peaks, also emphasize dual phased structures for very high nitrogen contents, see Figure 3c. All coatings investigated exhibit a more or less random orientation, independent on the prevalent nitrogen partial pressure. In summary, through the introduction of structural defects – being obvious in sputtering processes – the theoretical assumption that vacancies stabilize the cubic structure in TaC_xN_{1-x} and pure Ta_yN coatings could be clearly approved. The observed phase transition between single-phase fcc-structured TaC_xN_{1-x} and hexagonal coatings is around x = 0.32 being in excellent agreement to the theoretical predictions by DFT calculations, considering an error bar of the intersection between x = 0.20 to 0.42 – see Figure 2. In addition, for all single phase structured coatings the formation of amorphous C-N as well as C-C grain boundary phase seems to be immaterial.

To summarize the obtained structural and chemical data, we plotted all chemical compositions deposited in the Ta-rich section of the ternary Ta-C-N system, with indicated phase fields (shaded blue areas) after K. Frisk [8] calculated for 1400 °C. All fcc coatings are labeled by blue squares, whereas orange hexagon indicated dual phased coatings with minor hexagonal phase fractions. Only one composition indicated, $Ta_{0.51}C_{0.37}N_{0.12}$, lies within the fcc-$Ta_yC_xN_{1-x}$ phase field (equilibrium state), confirming the strong tendency to stabilize metastable phases throughout PVD. As the formation of amorphous grain boundary interior is a huge problem in the reactive deposition of carbide based thin films, we additionally evaluated amorphous free compositions by estimating the amount of C-C bonds for selected compositions utilizing XPS – see half-filled symbols within Figure 4. For $TaC_{0.71}$ around 6 % of the carbon atoms are characterized by only C-C bonds, indicating amorphous carbon based phase fractions. $Ta_{0.51}C_{0.37}N_{0.12}$ exhibit an even lower amount of around 4 %, whereas a further increase in the nitrogen content leads to more amorphous phase fractions up to 32 % for $Ta_{0.38}C_{0.20}N_{0.42}$. This is also in good agreement to the broadened XRD pattern for this specific coating. Except this coating, the spread between ERDA and XPS composition is almost constant. The indicated areas for the transition between fcc and hex structures, obtained by DFT (see magenta, green, and grey shaded areas), perfectly fit the experimental results. Due to calculational aspects, this areas were from compositional point of view evaluated in a very narrow field – meaning low amounts of vacancies – but can be conceptually extended.

To further proof the observed structural results, SEM and TEM investigations were conducted. In Figure 5a a representative bright field image of $Ta_{0.46}C_{0.32}N_{0.22}$ is given, exhibiting a highly dense and columnar structure. The SAED pattern plotted in Figure 5b confirms the XRD measurements, indicating a polycrystalline fcc-structured thin film. In addition, dark filed investigations reveal a columnar width of about 27 ± 5 nm for $Ta_{0.48}C_{0.31}N_{0.21}$ compared to 14 nm obtained during X-ray diffraction of the powdered coatings. Further TEM investigations on different compositions also feature the trend of smaller column width with increasing nitrogen content. Pure $TaC_{0.71}$ exhibits a larger column width of about 31 ± 6 nm. In addition, deposition rates were obtained out of the morphological investigations showing a clear decrease from 18.3 nm/min for pure Ar atmospheres, to 9 nm/min for $f_{[N_2]}^{norm}$ = 0.5. Increasing the bias potentials also slightly decrease the deposition rates, independent on the nitrogen partial pressure.

As the main concept of this work, is to tailor-made the mechanical properties of Ta-C thin films by substituting carbon through nitrogen, we also theoretical assessed this trend by ab initio calculations. Therefore, the elastic constants as well as polycrystalline bulk and shear modulus (B and G), Poisson ratio (ν), and Young's modulus, E, applying Hill's average [26] of the Reuss and Voigt bulk (B_R and B_V) and shear moduli (G_R and G_V), respectively were calculated – for details see Table 2. The detailed procedure of estimating B and G can be found elsewhere [27]. The obtained results for the calculated Young's modulus for fcc structured TaC_xN_{1-x} – utilizing also different potentials – are presented in Figure 6a. An increase of the nitrogen content clear decreases the Young's modulus from around 500 GPa for pure TaC to around 275 GPa for TaN, in relation to the used potentials. The results for the boarder systems fcc-Ta-C and fcc-Ta-N are in good agreement with values reported in literature (TaC [28], fcc-TaN [[9–29]). The slight deviations, especially for TaN, may also be related to the anisotropic behavior of this ceramic materials. The low anisotropy ratio of cubic TaC (0.6) and TaN (0.17) implies high anisotropy of the Young's modulus. From calculational point of view exhibits $TaC_{0.25}N_{0.75}$ the lowest anisotropy with an anisotropy ratio of 0.75 and 1.1 for LDA and PBE, respectively. Thus, texture can have a substantial influence on the mechanical properties of the films. Comparing now the theoretical predictions with experimentally observed indentation moduli – see red squares and hexagons in Figure 6a – we can find a highly similar trend. All experimental values shown in Figure 6 were obtained by films deposited on Silicon substrates with an applied bias

voltage of -10 V. The general offset of about 100 GPa can be either related to overestimating mechanical properties in DFT assuming perfect crystal with no morphological features as well as no textural consideration. The very short increase from $TaC_{0.71}$ to $Ta_{0.51}C_{0.37}N_{0.12}$ can be explained by the under stoichiometry of the Ta-C film, which lowers the elastic modulus [3]. In contrary, are literature data for TaN slightly higher as the measured and calculated values, being related to a textural effect, whereby the highest Young's modulus should be obtained for 100 direction. In addition, the deposited Ta-N obtains small amounts of hexagonal TaN, which is however reported to have a higher Young's modulus than fcc-TaN [30]. Next to the perfect agreement between calculated Young's modulus and experimentally observed values, also the hardness nicely fits this trend. From almost superhard $TaC_{0.71}$, 38.4 ± 1 GPa, the hardness linearly decreases to around 25 GPa for $Ta_{0.38}C_{0.20}N_{0.42}$. Here, again the maybe dual phase structure could slightly influence the mechanical properties, but still the trend is evident. Furthermore, the substitution of carbon through nitrogen also decreases the highly compressed state of the films from -4.0 GPa for $TaC_{0.71}$ to -1.75 for $Ta_{0.38}C_{0.20}N_{0.42}$, respectively. The difference in stress and hardness loss – over 10 GPa for the hardness compared to 2 GPa for the residual stresses - is a further proof for the intrinsic property adjustment through alloying nitrogen on the non-metallic sublattice. In addition, increasing bias potentials only (-90 V) increase the residual stress to around -4.63 GPa. Taking all this into account the experimentally determined and calculated trends of the mechanical behavior are in very good accordance. At this point, we have to mention that a different behavior is reported by S. Du et al [11]. However, S. Pugh proposed an empirical relationship between ductile and brittle behavior of a material and considered this as the B/G ratio (Pugh-ratio) [31]. A high (low) value of B/G is associated with ductility (brittleness). The critical value separating brittle and ductile materials is commonly referred to around 1.75. Our calculations propose that the substitution of C atoms with N in the investigated TaC_xN_{1-x} supercells leads to an increase in ductility. The transition from brittle to ductile behavior is at around $TaC_{0.67}N_{0.33}$ (LDA) and $TaC_{0.62}N_{0.38}$ (PBE), respectively. Single cantilever bending tests, confirm this prediction and will be discussed in more detail in a further study.

Next to the circumstance that alloying of N to form solid solutions of TaC_xN_{1-x} allows for adjusting the mechanical properties towards a more damage tolerant character, it is also suggested to even increase the bonding strength exhibiting maybe higher melting

temperatures as the binary counterparts [32]. To investigate this behavior, we conducted different annealing tests on powdered coatings as well as thin films deposited on sapphire substrates. Two Ta-C-N coating powders deposited at $f_{[N_2]}^{norm}$= 0.1 but with different bias potentials (-10 V and -60 V) are compared to pure $TaC_{0.71}$ (U_{Bias} = -10 V) – see Figure 7. The thermo-gravimetry signal, illustrated as mass change [%] in Figure 7a, shows a stronger mass loss for both $Ta_{0.46}C_{0.32}N_{0.22}$ powders compared to pure $TaC_{0.71}$. While the mass loss sets in at the temperature range of about 1280°C for the $Ta_{0.46}C_{0.32}N_{0.22}$ coatings, it can be detected at around 1350 °C for the binary counterpart. The coating deposited at higher bias potential reveals a reduced mass loss of about -3.7 % compared to -4.2 %, indicating that the thermal stability can even be increased through the surface mobility during film growth. However, the predicted increase of thermal stability, and hence melting temperature, could not be recognized within this test series. In Figure 7b, the structural data for the $Ta_{0.46}C_{0.32}N_{0.22}$ coating deposited at -10 V are compared in the as deposited and annealed state. Hexagonal -$Ta_2(C,N)_x$ phase rises due to annealing. Considering the calculated phase areas [8] in the ternary system, we assume that the mass loss is caused by a loss of C and N . This leads to an increasing Ta content and hence the formation of hex-$Ta_2(C,N)_x$ phase fractions. Ta_2C based structures also reveal a lowered energy of formation compared to fcc structured Ta-C and hence is maybe promoted during decomposition. However, the slightly decreased thermal stability is good agreement to the reduced mechanical properties with increasing N contents, suggesting a reduction of covalent bonding character. Assuming there is an equal loss of C and N, and all residual Ar within the film is gone, the new composition for the -10 V coating would be around $Ta_{0.61}C_{0.26}N_{0.13}$. This composition is right in the middle of the two phase fields (fcc-$Ta_YC_xN_{1-x}$ and hex-$Ta_2(C,N)_x$) in Figure 4, which matches the phase composition. The standard deviation for the residual Ar has a substantial influence on this calculation which – as well as an unknown error of the mass loss – makes an accurate calculation impossible. Although the as deposited composition of $TaC_{0.71}$ is already located in the two-phase field, the amount of Ta_2C phase in the as deposited and annealed $TaC_{0.71}$ is much lower compared to annealed Ta-C-N. In addition, a different study [3] proposed $TaC_{0.76}$ to be the most stable composition.

Furthermore, $Ta_{0.46}C_{0.32}N_{0.22}$ and $TaC_{0.71}$ deposited on sapphire substrate were also comparative annealed from 600 °C to 1400 °C. Visual inspection of the thin films after annealing reveals a change of color for samples annealed at increasing temperatures. We

further see delamination effects for $Ta_{0.46}C_{0.32}N_{0.22}$ at 1200 °C as well as $TaC_{0.71}$ at 1400 °C, respectively. Corresponding XRD patterns show that on sapphire substrates TaC_y prefers being oriented in (100) direction, whereas $Ta_{0.46}C_{0.32}N_{0.22}$ on sapphire exhibits 220 texture. Furthermore, the 220 peak is shifted to lower 2theta compared to the TaC reference, which corresponds to high compressive stresses within the film. With increasing annealing temperature, the 220-peak shifts to higher 2theta accompanied with a decrease of the integral breadth. This is a sign for re-crystallization, which also leads to a decrease of compressive stress and therefore a peak shift to higher 2theta values. This effect is growing with increasing annealing temperature. For TaC_y this relaxation is less pronounced. However, both samples annealed at 1400 °C show a big amount of Ta_2C as expected from the powder annealing tests. Nanoindentation up to an annealing temperature of 1000 °C show that both $Ta_{0.46}C_{0.32}N_{0.22}$ and $TaC_{0.71}$ retain their supreme hardness (Figure 8). For 1000 °C, measurements even suggest superior hardness of $Ta_{0.46}C_{0.32}N_{0.22}$. The much higher hardness measured here compared to the films on silicon substrate in Figure 7b (+4 GPa and +1.5 GPa) is associated to higher compressive stresses. It should be noted that indentation depths were below 10% of the film thickness, which is reported to be sufficient to extinguish substrate interference [33]. Furthermore, indentation modulus is more strongly affected by the substrate [33] which explains the different values.

Conclusion

In summary, we investigated the concept of non-metallic alloying on the specific sublattice in fcc structured transition metal carbides, by substituting carbon with nitrogen atoms, forming Ta-C-N structures. The ab initio inspired predictions were experimentally proven by magnetron sputtered Ta-C-N thin films. Throughout this concept, the thermomechanical properties are adjusted towards a more ductile character.

DFT based calculations highlighted, that the preferred vacancy species can be tuned with changing the sublattice compositions. Nitrogen rich compositions prefer metal vacancies, whereas non-metallic defects are promoted on the Ta-C side within the ternary system. Through this effect, the phase field for fcc-structured Ta-C-N can be extend up to nitrogen contents of about 65 % on the non-metallic sublattice. This theoretical prediction was found to be in excellent agreement with composition and structure analysis of sputter deposited TaC_xN_{1-x} thin films. The theoretical transition between fcc and hex crystal is observed at about

x = 0.40 to 0.20, whereas as for our synthesized films it reaches x = 0.32. The corresponding mechanical properties, also perfectly fit the ab-initio results, that the hardness and indentation modulus decreases from experimentally 40 to 25 GPa as well as 360 to 250 GPa for $TaC_{0.71}$ to $TaC_{0.32}N_{0.68}$, respectively. The calculated Young's modulus also linearly decreases from 500 to 250 GPa in the full compositional range, slightly overestimating these experimentally values. The decrease in hardness is also accompanied by a stress relaxation from around -4.0 to -1.5 GPa for $TaC_{0.71}$ to $TaC_{0.32}N_{0.68}$, which also highlights adapting the mechanical properties on an atomic scale range. In accordance with a slightly reduced thermal stability, meaning phase degradation detected around 1300 in DSC/TG analysis, this indicates a reduced bonding strength hence a reduced covalent and more metallic like bonding character. Pugh's semi-empirical criterion for ductility (B/G > 1.75) even suggest ductile behavior with the addition of nitrogen. However, through the introduction of nitrogen the thermomechanical properties of Ta-C-N also exceeds Ta-C obtain around 38 GPa even after annealing at 1000 °C, compared to 32 GPa for pure $TaC_{0.71}$.

Nevertheless, this study emphasizes an alternative alloying concept for ceramic like thin film materials, by forming solid solutions on the non-metallic sublattice. The investigated Ta-C-N system gives a promising prospective for further ultra-high temperature ceramics.

Acknowledgement

We thank the Vienna Scientific Cluster for the attribution of computation time, the X-ray center of TU Wien for beam time, the USTEM center of TU Wien for the SEM and TEM facilities, as well as the Swedish Foundation for Strategic Research, which supported the accelerator operation at Uppsala University.

Figure captions

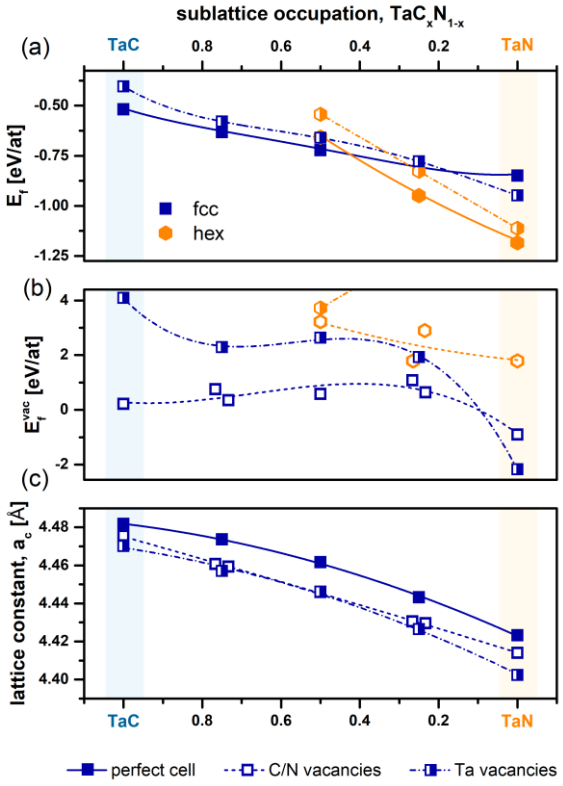

Figure 1: Phase transition observing ab initio calculated, E_f, between fcc and hex structured TaC_xN_{1-x} utilizing perfect and metal deficient super cells (a). Energy of formation for specific vacancy types, E_f^{vac}, over the full compositional range. Calculated lattice constants of perfect and defected fcc structured TaC_xN_{1-x} (c). Blue squares denote to fcc structured TaC_xN_{1-x}, whereas orange hexagons indicated hexagonal structures.

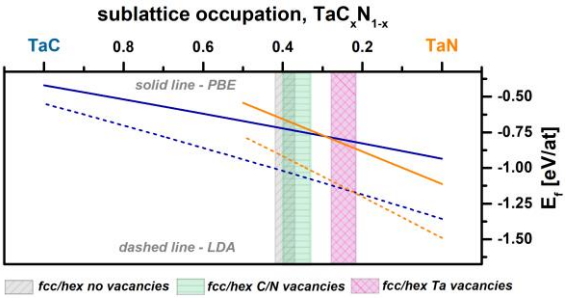

Figure 2: Phase intersection between fcc and hex TaC_xN_{1-x} structure influenced by vacancies as well as different potentials utilized. The colored regions represent an error bar for this intersection, considering the different vacancy species types, obtained by PBE (left border) and LDA (right border) calculations. Solid and dashed lines show the E_f curve for the perfect and Ta vacant (vacancy concentration of 6%) cells for PBE and LDA potential, respectively.

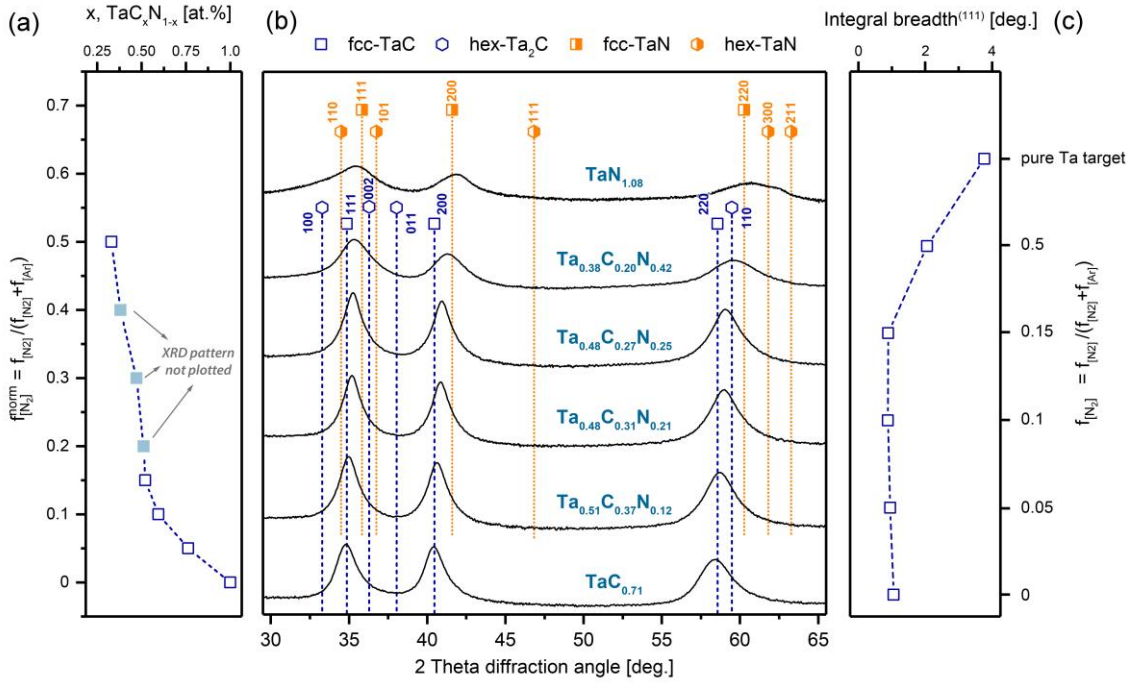

Figure 3: (a) Relationship between the deposition conditions (nitrogen to total flow rate) and the carbon to nitrogen ratio, x. XRD phase analysis of powdered coatings in as deposited state with in increasing nitrogen content (b) – see Figure 3a. (c) Integral breadth of the (111) peak (b) for corresponding $f_{[N_2]}^{norm}$.

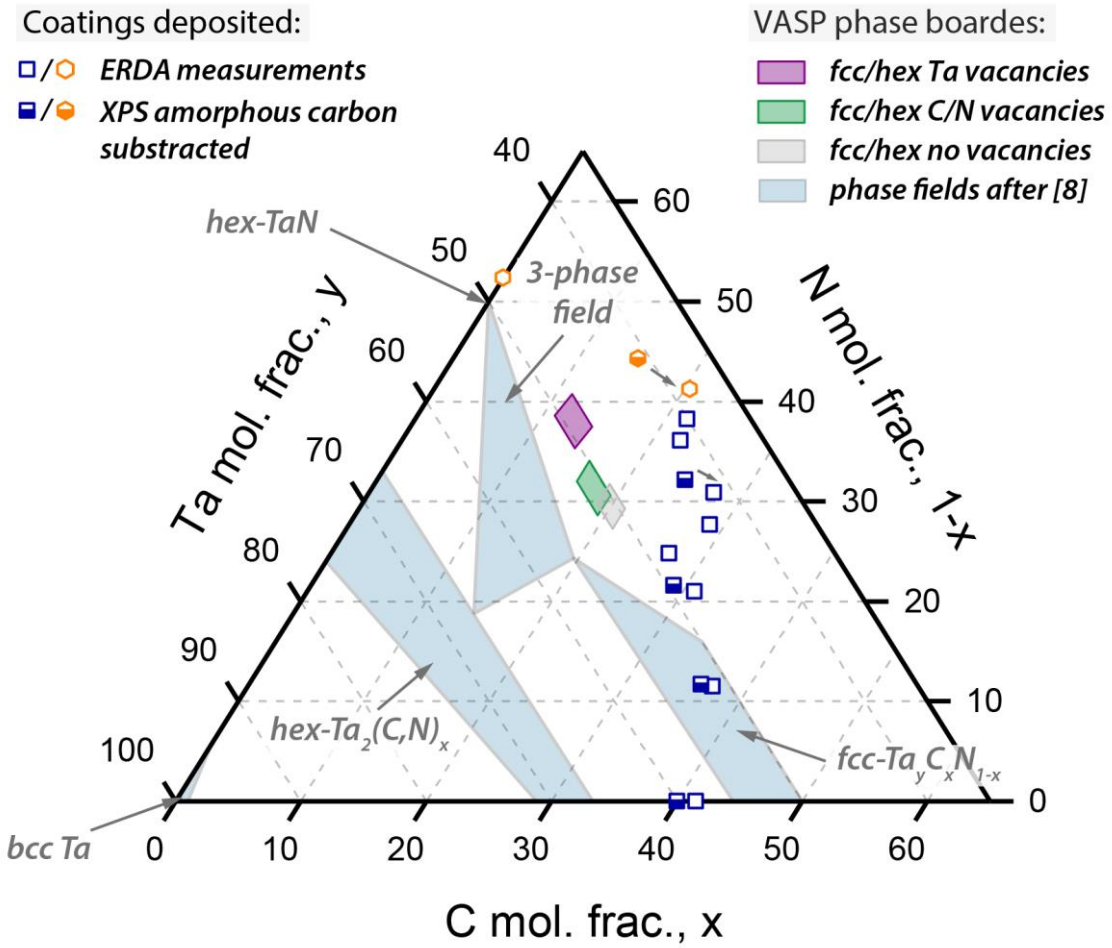

Figure 4: Ta-C-N ternary phase diagram, with indicated phase fields reported by K. Frisk [8] at 1400 °C. The ab initio obtained phase fields, see Figure 2, are also indicated within the system. Open symbols represent compositions obtained by ERDA, whereas half-filled symbols are corrected by the amount of amorphous carbon based on XPS measurements.

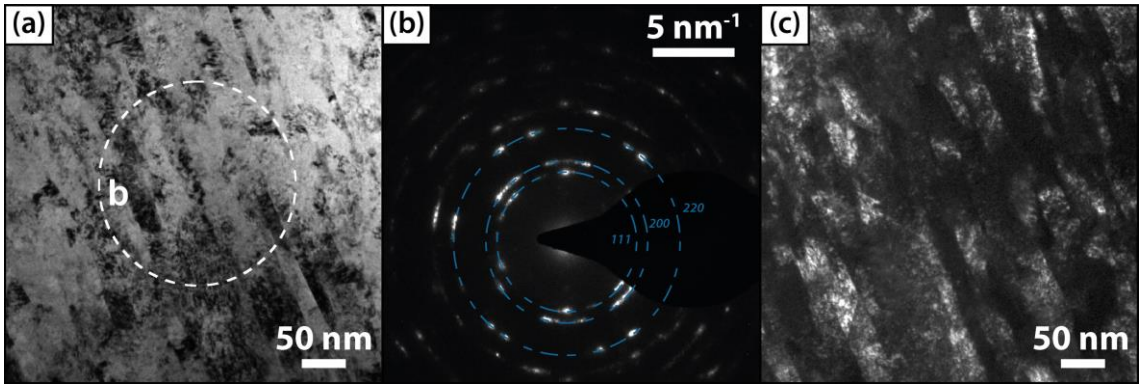

Figure 5: TEM bright field (BF) (a), with the corresponding SAED-pattern presented in (b). In addition, a dark field (DF) image for the $Ta_{0.46}C_{0.32}N_{0.22}$ is presented in (c).

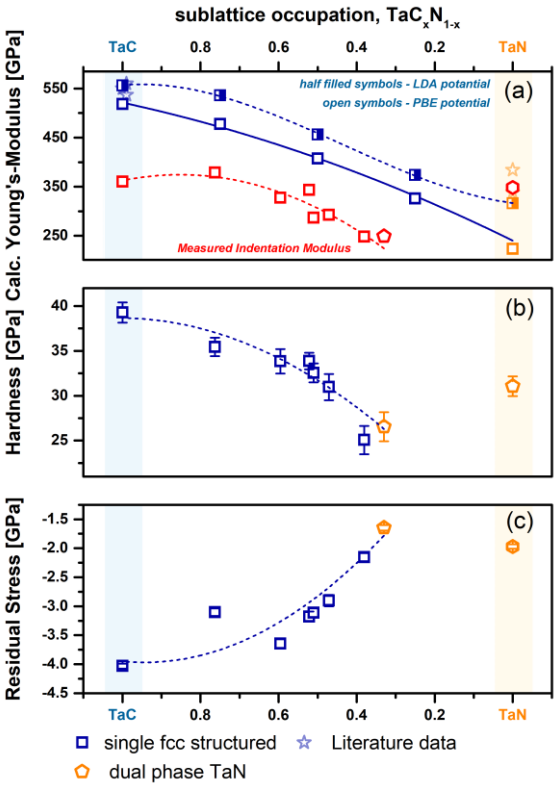

Figure 6: (a) VASP calculated Young's-Modulus for fcc structured TaC_xN_{1-x} utilizing different potentials, PBE and LDA, compared to literature and experimentally data (red symbols) determined by nanoindentation. (b) Indentation hardness (b) as well as residual stress (c) in relation to the observed sublattice occupation. Hexagons indicate dual phased fcc/hex Ta(C,N) structures.

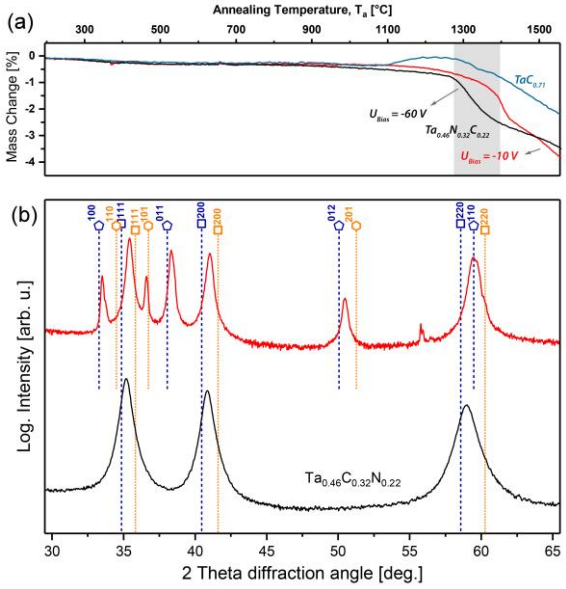

Figure 7: (a) TG measurements for films deposited with same nitrogen partial pressure, $f_{[N_2]}^{norm}$= 0.1, but different bias voltage applied. For comparison, also the mass change in relation to temperature is given for $TaC_{0.71}$. Phase analysis of $Ta_{0.46}C_{0.32}N_{0.22}$ (-60 V) before (lower pattern) and after annealing (upper pattern, red).

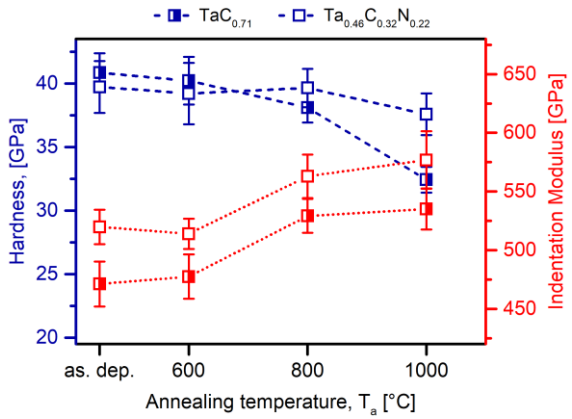

Figure 8: Hardness and Indentation modulus evolution with increasing annealing temperatures. All coatings were deposited on sapphire substrates.

Appendix

Table 1
Chemical composition of the coatings obtained by ERDA analysis with the corresponding deposition parameters. The average error ranges between 1 and 2% of the presented mean atomic fractions.

Sample	Deposition parameters				C/(N+C)	Elements (at. %)		
	Bias potential	$f_{[N_2]}^{norm}$	Ar	N_2	x	Ta	C	N
	[V]		[sccm]					
$TaC_{0.71}$	-10	0	20	0	-	0.585	0.415	-
$Ta_{0.51}C_{0.37}N_{0.12}$	-10	0.05	19	1	0.76	0.514	0.371	0.115
$Ta_{0.47}C_{0.34}N_{0.19}$ [1]	-75	0.05	19	1	0.64	0.466	0.344	0.190
$Ta_{0.48}C_{0.31}N_{0.21}$	-10	0.1	18	2	0.60	0.481	0.309	0.210
$Ta_{0.46}C_{0.32}N_{0.22}$ [2]	-60	0.1	18	2	0.59	0.459	0.320	0.221
$Ta_{0.48}C_{0.27}N_{0.25}$	-10	0.15	17	3	0.52	0.482	0.270	0.248
$Ta_{0.43}C_{0.29}N_{0.28}$	-10	0.2	16	4	0.51	0.435	0.288	0.276
$Ta_{0.42}C_{0.27}N_{0.31}$	-10	0.3	14	6	0.47	0.416	0.275	0.309
$Ta_{0.42}C_{0.22}N_{0.36}$	-10	0.4	12	8	0.38	0.417	0.222	0.361
$Ta_{0.38}C_{0.20}N_{0.42}$	-10	0.5	10	10	0.33	0.383	0.203	0.414
$TaN_{1.08}$	-10	0.5	10	10	-	0.476	-	0.524

[1] Film was deposited at a heater temperature of 730°C and power density of 0.75 W/cm^2

[2] Different bias potential was applied to study its effect on thin film morphology and hardness

Table 2
TaC_xN_{1-x} DFT calculations using to different exchange correlation potential approximations, PBE and LDA. Table show lattice constant (a), elastic constants of stiffness tensor (C_{11} C_{12} C_{44}), G, B, E moduli (in GPa), Poisson's ratio (v) and Pugh's ratio (B/G)

	x	a	C_{11}	C_{12}	C_{44}	G	B	E	v	B/G
PBE	1	4.482	702	139	172	210	328	518	0.24	1.56
	0.75	4.474	658	141	157	192	314	478	0.25	1.64
	0.5	4.462	585	169	133	159	308	407	0.28	1.94
	0.25	4.443	513	222	110	123	318	327	0.33	2.59
	0	4.423	672	162	42	95	333	260	0.37	3.51
LDA	1	4.421	768	157	181	224	361	556	0.24	1.61
	0.75	4.409	769	144	167	215	353	536	0.25	1.64
	0.5	4.395	684	183	141	178	349	456	0.28	1.96
	0.25	4.375	589	254	125	141	366	374	0.33	2.61
	0	4.356	792	173	52	116	379	316	0.36	3.26

References

1. P. H. Mayrhofer, A. Hörling, L. Karlsson, J. Sjölén, T. Larsson, C. Mitterer, & L. Hultman, Self-organized nanostructures in the Ti-Al-N system. *Applied Physics Letters*, **83** (2003) 2049–2051. https://doi.org/10.1063/1.1608464.
2. O. Cedillos-Barraza, D. Manara, K. Boboridis, T. Watkins, S. Grasso, D. D. Jayaseelan, R. J. M. Konings, M. J. Reece, & W. E. Lee, Investigating the highest melting temperature materials: A laser melting study of the TaC-HfC system. *Scientific Reports*, **6** (2016) 37962. https://doi.org/10.1038/srep37962.
3. H. Riedl, T. Glechner, T. Wojcik, N. Koutná, S. Kolozsvári, V. Paneta, D. Holec, D. Primetzhofer, & P. H. Mayrhofer, Influence of carbon deficiency on phase formation and thermal stability of super-hard TaC y thin films. *Scripta Materialia*, **149** (2018) 150–154. https://doi.org/10.1016/j.scriptamat.2018.02.030.
4. R. Bermejo, R. Daniel, C. Schuecker, O. Paris, R. Danzer, & C. Mitterer, Hierarchical Architectures to Enhance Structural and Functional Properties of Brittle Materials. *Advanced Engineering Materials*, **19** (2017). https://doi.org/10.1002/adem.201600683.
5. R. Hahn, M. Bartosik, R. Soler, C. Kirchlechner, G. Dehm, & P. H. Mayrhofer, Superlattice effect for enhanced fracture toughness of hard coatings. *Scripta Materialia*, **124** (2016) 67–70. https://doi.org/10.1016/j.scriptamat.2016.06.030.
6. V. Moraes, H. Riedl, C. Fuger, H. Bolvardi, P. Polcik, D. Holec, & P. H. Mayrhofer, Ab-initio inspired design of ternary boride thin films. *submitted to Scientific Reports*, (2018).
7. M. Grumski, P. P. Dholabhai, & J. B. Adams, Ab initio study of the stable phases of 1:1 tantalum nitride. *Acta Materialia*, **61** (2013) 3799–3807. https://doi.org/10.1016/j.actamat.2013.03.018.
8. K. Frisk, Analysis of the phase diagram and thermochemistry in the Ta–N and the Ta–C–N systems. *Journal of Alloys and Compounds*, **278** (1998) 216–226. https://doi.org/10.1016/S0925-8388(98)00582-9.
9. N. Koutná, D. Holec, M. Friák, P. H. Mayrhofer, & M. Šob, Stability and elasticity of metastable solid solutions and superlattices in the MoN-TaN system: a first-principles study. (2017) 1–12.

10. X. Yu, G. B. Thompson, & C. R. Weinberger, Influence of carbon vacancy formation on the elastic constants and hardening mechanisms in transition metal carbides. *Journal of the European Ceramic Society*, **35** (2015) 95–103. https://doi.org/10.1016/j.jeurceramsoc.2014.08.021.

11. S. Du, K. Zhang, Q. Meng, P. Ren, C. Hu, M. Wen, & W. Zheng, N dependent tribochemistry: Achieving superhard wear-resistant low-friction TaC x N y films. *Surface and Coatings Technology*, **328** (2017) 378–389. https://doi.org/10.1016/j.surfcoat.2017.09.006.

12. S. M. Aouadi, Y. Zhang, P. Basnyat, S. Stadler, P. Filip, M. Williams, J. N. Hilfiker, N. Singh, & J. A. Woollam, Physical and chemical properties of sputter-deposited TaC x N y films. *Journal of Physics: Condensed Matter*, **18** (2006) 1977–1986. https://doi.org/10.1088/0953-8984/18/6/013.

13. H. Lasfargues, T. Glechner, C. M. Koller, V. Paneta, D. Primetzhofer, S. Kolozsvári, D. Holec, H. Riedl, & P. H. Mayrhofer, Non-reactively sputtered ultra-high temperature Hf-C and Ta-C coatings. *Surface and Coatings Technology*, **309** (2017) 436–444. https://doi.org/10.1016/j.surfcoat.2016.11.073.

14. P. Ström, P. Petersson, M. Rubel, & G. Possnert, A combined segmented anode gas ionization chamber and time-of-flight detector for heavy ion elastic recoil detection analysis. *Review of Scientific Instruments*, **87** (2016) 103303. https://doi.org/10.1063/1.4963709.

15. Y. Zhang, H. J. Whitlow, T. Winzell, I. F. Bubb, T. Sajavaara, K. Arstila, & J. Keinonen, Detection efficiency of time-of-flight energy elastic recoil detection analysis systems. *Nuclear Instruments and Methods in Physics Research Section B: Beam Interactions with Materials and Atoms*, **149** (1999) 477–489. https://doi.org/10.1016/S0168-583X(98)00963-X.

16. W. C. Oliver & G. M. Pharr, An improved technique for determining hardness and elastic modulus using load and displacement sensing indentation experiments. *Journal of Materials Research*, **7** (1992) 1564–1583. https://doi.org/10.1557/JMR.1992.1564.

17. G. C. A. M. Janssen, M. M. Abdalla, F. van Keulen, B. R. Pujada, & B. van Venrooy, Celebrating the 100th anniversary of the Stoney equation for film stress: Developments from polycrystalline steel strips to single crystal silicon wafers. *Thin Solid Films*, **517** (2009) 1858–1867. https://doi.org/10.1016/J.TSF.2008.07.014.

18. G. Kresse & J. Furthmüller, Efficient iterative schemes for *ab initio* total-energy calculations using a plane-wave basis set. *Physical Review B*, **54** (1996) 11169–11186. https://doi.org/10.1103/PhysRevB.54.11169.

19. G. Kresse & D. Joubert, From ultrasoft pseudopotentials to the projector augmented-wave method. *Physical Review B*, **59** (1999) 1758–1775. https://doi.org/10.1103/PhysRevB.59.1758.

20. W. Kohn & L. J. Sham, Self-Consistent Equations Including Exchange and Correlation Effects. *Physical Review*, **140** (1965) A1133–A1138. https://doi.org/10.1103/PhysRev.140.A1133.

21. J. P. Perdew, K. Burke, & M. Ernzerhof, Generalized Gradient Approximation Made Simple. *Physical Review Letters*, **77** (1996) 3865–3868. https://doi.org/10.1103/PhysRevLett.77.3865.

22. S.-H. Wei, L. G. Ferreira, J. E. Bernard, & A. Zunger, Electronic properties of random alloys: Special quasirandom structures. *Physical Review B*, **42** (1990) 9622–9649. https://doi.org/10.1103/PhysRevB.42.9622.

23. R. Yu, J. Zhu, & H. Q. Ye, Calculations of single-crystal elastic constants made simple. *Computer Physics Communications*, **181** (2010) 671–675. https://doi.org/10.1016/j.cpc.2009.11.017.

24. N. Koutná, D. Holec, O. Svoboda, F. F. Klimashin, & P. H. Mayrhofer, Point defects stabilise cubic Mo-N and Ta-N. *Journal of Physics D: Applied Physics*, **49** (2016) 375303. https://doi.org/10.1088/0022-3727/49/37/375303.

25. N. Bohr, I. On the constitution of atoms and molecules. *The London, Edinburgh, and Dublin Philosophical Magazine and Journal of Science*, **26** (1913) 1–25.

26. R. Hill, The elastic behaviour of a crystalline aggregate. *Proceedings of the Physical Society. Section A*, **65** (1952) 349–354. https://doi.org/10.1088/0370-1298/65/5/307.

27. F. Tasnádi, M. Odén, & I. A. Abrikosov, Ab initio elastic tensor of cubic Ti 0.5Al 0.5N alloys: Dependence of elastic constants on size and shape of the supercell model and their convergence. *Physical Review B - Condensed Matter and Materials Physics*, **85** (2012) 1–9. https://doi.org/10.1103/PhysRevB.85.144112.

28. L. López-De-La-Torre, B. Winkler, J. Schreuer, K. Knorr, & M. Avalos-Borja, Elastic properties of tantalum carbide (TaC). *Solid State Communications*, **134** (2005) 245–250. https://doi.org/10.1016/j.ssc.2005.01.036.

29. J. Chang, G. Zhao, X. Zhou, K. Liu, & L. Lu, Structure and mechanical properties of tantalum mononitride under high pressure : A first-principles study Structure and mechanical properties of tantalum mononitride under high pressure : A first-principles study. **83519** (2012). https://doi.org/10.1063/1.4759279.

30. E. Zhao, B. Hong, J. Meng, & Z. Wu, First principles investigation on the ultra-incompressible and hard TaN. *Journal of Computational Chemistry*, **30** (2009) 2358–2363. https://doi.org/10.1002/jcc.21234.

31. S. F. Pugh, XCII. Relations between the elastic moduli and the plastic properties of polycrystalline pure metals. *The London, Edinburgh, and Dublin Philosophical Magazine and Journal of Science*, **45** (1954) 823–843. https://doi.org/10.1080/14786440808520496.

32. Q.-J. Hong & A. van de Walle, Prediction of the material with highest known melting point from ab initio molecular dynamics calculations. *Physical Review B*, **92** (2015) 20104. https://doi.org/10.1103/PhysRevB.92.020104.

33. R. Saha & W. D. Nix, Effects of the substrate on the determination of thin mechanical properties by nanoindentation. *Acta Materialia*, **50** (2002) 23–28. https://doi.org/10.1016/S1359-6454(01)00328-7.

Publication II

How to improve the ductile behavior of superhard Ta-C-N thin films

T. Glechner, S. Kolozsvári, H. Zaid, S. Kodambaka, P. H. Mayrhofer and H. Riedl

(April 2018, manuscript in final preparation)

How to improve the ductile behavior of superhard Ta-C-N thin films

T. Glechner[a], R. Hahn[a], T. Wojcik[a], S. Kolozsvári[b], H. Zaid[c], S. Kodambaka[c], P. H. Mayrhofer[a], and H. Riedl[a]

[a] Institute of Materials Science and Technology, TU Wien, A-1060 Wien, Austria

[b] Plansee Composite Materials GmbH, D-86983 Lechbruck am See, Germany

[c] Department of Materials Science and Engineering, University of California Los Angeles, Los Angeles, CA 90095, USA

Based on the concept of non-metal alloying – by substituting C with N atoms – in Ta-C based coatings, we could show a clear enhancement of the rather low ductility of this super-hard coating material. The effect is studied in detail by a combined experimentally and theoretical approach on sputter deposited 110-oriented $Ta_{0.47}C_{0.34}N_{0.19}$ films. Although the film exhibits super-hardness (43.3±1.4 GPa) plastic deformation is observed in micro-pillar compression tests over a yield stress, σ_Y, of 16.89±1.39 GPa with {111}<$01\bar{1}$> as the most active slip system. Furthermore, superior fracture toughness of Ta-C-N compared to Ta-C is proofed by cantilever testing. Our results give a rather promising perspective on how ductility of ultra-high temperature ceramics can be enhanced by adapting the bonding state on the non-metallic sub-lattice.

Keywords: Ta-C-N; Thin films; Density Functional Theory; Fracture Toughness; Carbonitrides;

***Corresponding author's e-mail address:** thomas.glechner@tuwien.ac.at

Introduction

Transition metal (TM) carbides and nitrides are well established in various industrial applications – especially as thin films – due to their outstanding properties including highest melting temperatures, extreme hardness and chemical inertness. They exhibit a mixture of strong ionic, covalent, and metallic bonds but possess a very low ductile character, which primarily limits their application as structural components as well as thin films. Therefore, improving ductility while retaining other thermo-mechanical properties is a major motivation for research done on TM ceramics. For thin film materials, enhanced damage tolerance can be gained through e.g. metal alloying concepts [1], phase architecture through so-called tissue phases, or architectural arrangements such as introducing metallic layers or hierarchical structures, which lead to more or less toughness enhancements [2–4] – K_{IC} increases by one order of magnitude. In this study, however, we are interested on an intrinsic increase of ductility through adapting the bonding character of our coating material [5].

Among TM carbides, Ta-C exhibits highly interesting material properties such as highest melting temperature of all binary systems known (3983 °C [6]) or extremely high electrical conductivity for ceramic materials (>5 x 10^6 Ω^{-1} m^{-1} at 300 K [7]). Furthermore, Ta-C has been proven to be super-hard [8], but highly brittle in temperature ranges below $0.5 \cdot T_m$ – fracture appearance transition temperature is at least $0.4 \cdot T_m$ or higher. However, compared to other TM carbides, Ta-C still appears to have a more metallic nature, leading to unique mechanical characteristics in single crystals, as these crystals behave in a relatively ductile manner and deform plastically before cracking [9]. Therefore, Ta-C seems to be a very promising choice among TM carbides to experience plastic deformation and thus ductility. To adjust the properties of Ta-C on an atomistic level and possibly gain even higher damage tolerance, a highly attractive method is the partly substitution of carbon by nitrogen atoms on the non-metallic sublattice – meaning a kind of solid solution. Motivated by our previous work [10], we experimentally proofed that the incorporation of nitrogen decreases the elastic modulus and hardness. In addition, ab initio based calculations estimating the elastic constants, reveal that the Pugh ratio undergoes a transition to the ductile regime with increasing nitrogen content. However, the authors want to mention, that the idea of combining nitride and carbide based TM is not completely new [11–13], but tailoring thin film properties by forming specific non-metallic solutions has a novel character. To determine mechanical properties of

small-scale materials, various methods were invented, whereas in-situ nanoindentation in different loading directions and geometries represents the most important method. Especially, micro-pillar compression testing as invented by Uchic et al. [14] but also bending-tests utilizing micro-cantilevers are most prevalent. However, a comparative use of different methods is highly recommend to assess absolute values [15]. Micro-pillar compression tests on Ta-C crystals revealed shear deformation with slip systems activate, suffering highest resolved shear stress [16].

In this work, we want to extend the knowledge on the deformation behavior and mechanical properties of Ta-C-N ceramics, synthesized as thin films. Therefore, micro-pillar compression tests as well as micro-cantilever testing were correlated with nanoindentation on Ta-C as well Ta-C-N coatings. In addition, to gain a deep in-sight on adapting the bonding character by substituting C with N atoms, accompanying ab initio calculations were conducted.

Experimental procedures

The Ta-C-N film was deposited in a UHV sputtering deposition system (AJA orion 5) using a 3-inch $TaC_{0.97}$ compound target (Plansee Composite Materials GmbH [17]). The target was operated in pulsed DC-mode and DC bias potential of -75V was applied to the substrate. Heater temperature was set to 730 °C corresponding to about 550±10 °C at the substrate materials. The film was deposited in a mixed Ar/N_2 atmosphere, at a total gas flow of 20 sccm and a working pressure of 0.4 Pa. The ratio between the argon and nitrogen flow rate was set to 0.05. We utilized polished single crystalline sapphire (Crys Tec (1-102)-orientation) platelets as substrate materials.

Structural investigations were done by X-ray diffraction (XRD) in Bragg Brentano configuration applying a Panalytical Empyrean diffractometer equipped with a Cu-K_α radiation source (wave length λ = 1.54 Å). Structure and morphology of the film was further investigated applying cross sectional analysis in a transmission electron microscope (TEM FEI TECNAI F20, field emission gun, acceleration voltage of 200 kV). Nanoindentation was carried out on a UMIS system, equipped with a Berkovich diamond tip. Load displacement curves (25) at different loads (varying between 45 to 3 mN), were recorded and analyzed after Oliver and Pharr [18]. Cylindrical pillars for micro-pillar compression tests and pillar splitting tests were prepared by

using a focused ion beam (FIB) system (FEI Nova 600 SEM/FIB). A two-step process of initial coarse milling with an ion-current of 1 nA followed by fine milling with a 30 pA current was applied. Using this process, we obtained pillars with a taper angle < 5 ° (compression tests) and < 3 ° (pillar splitting). For pillar splitting tests, pillars exhibited an aspect ratio, h/D of around 1 and a top diameter that is slightly larger compared to the film thickness (h refers to the pillar height and D represents the top diameter of the pillar). This geometry assures surface residual stress relaxation [19].

For in-situ cantilever beam bending tests 7 beams, with dimension of about 960x910x6250 nm^3, were FIB milled in a two-step process (used FIB work station: FEI Quanta 200 3D DBFIB). As a first step, the substrate materials was removed, and secondly final beam dimensions were gained by milling perpendicular to the film surface. Coarse milling was conducted at 1 nA, whereas fine milling was conducted at 0.5 nA, respectively. The pre-notch was milled using 50 pA. Pillars and cantilevers were loaded inside the SEM/FIB system using a picoindenter (PI 85 Hysitron) in displacement control mode. For the micro-pillar compression tests, the indenter was equipped with a 5 µm wide flat diamond punch – loading rate of 5 nm/s was applied. For pillar splitting a cube corner tip (200 nm diameter, loading rate 10 nm/s) as well as for cantilever beam bending a spherical diamond tip was utilized (tip radius of around 1 mm, loading rate 5 nm/s). During all experiments, the load displacement data has been recorded self-controlled.

Computational details

To investigate mechanical properties of TaC_xN_{1-x}, density functional theory (DFT) calculations have been performed with VASP (Vienna ab initio simulation package) [20,21] using the projector augmented plane wave (PAW) pseudopotentials. Two different exchange correlation potential approximations, Local density Approximation (LDA) and the generalized gradient approximation (GGA) [22] with a Perdew-Burke-Ernzerhof (PBE) exchange correlation functional [23] have been utilized. We investigated the crystal structure of face centered cubic Ta-C and Ta-N ($Fm\bar{3}m$, #225). To design the required supercells, the special quasirandom structure (SQS) method [24] was used to introduce vacancies. The elastic constants were obtained applying the universal linear-independent coupling strain (ULICS) method [25]. For further details on the methodology used for the calculations please see [10].

Results and Discussion

To assess the ductile character of various TaC_xN_{1-x} compositions (step size of x = 0.25 applied), especially with respect to increasing nitrogen content, we employed the two classical semi-empirical criteria after Pettifor [26] and Pugh [27]. Therefore, the Cauchy pressure, C_{12}-C_{44}, is plotted against the Pugh ratio B/G – see Figure 1. This data was recalculated applying Hill's average [28] of the Reuss and Voigt bulk (B_R,B_V) and shear moduli (G_R,G_V), polycrystalline bulk modulus, B, shear modulus, G, Poisson ratio, v, and Young's modulus, E - for further calculation details see [29]. All ternary coatings are labeled with orange symbols, whereby the binary counterparts are indicated by blue ones. Considering the influence of different potentials applied in the DFT calculations, half-filled and open squares refer to LDA and PBE, respectively. In addition, the influence of non-metallic vacancies is also incorporated – randomly distributed C/N vacancies 6 % - and indicated by triangle symbols in Figure 1. The experimentally deposited thin film, obtaining a composition of $Ta_{0.47}C_{0.34}N_{0.19}$ (further details presented in [10]), which corresponds to x =0.64 (C/(C+N), is labeled through red symbols. The deviation of the calculated composition, $TaC_{0.625}N_{0.375}$, is based on the limited supercell size, but still in good agreement. However, materials with C_{12}-C_{44} > 0 and B/G > 1.75 are considered as ductile. Figure 1 clearly shows that increasing nitrogen in TaC_xN_{1-x} increases the Cauchy pressure as well as Pugh ratio, which is associated with an increase of ductility. The composition of the film used in this work is therefore already in the ductile regime. Furthermore, C/N vacancies have only a minor influence on the brittle to ductile transition for x = 0.75 and x = 0.50. In pure TaC, our calculations even suggest higher brittleness when introducing carbon vacancies. This is maybe in good agreement to the anomalous hardness increase known for under stoichiometric TaC_y [8]. For N rich TaC_xN_{1-x} and pure TaN, the influence of vacancies obtains no clear trend, but still highly ductile character. However, we need to mention Koutna et al. reported a slightly smaller B/G ratio (2.69) compared to this work.

As already mentioned, TaC as well as TaN obtains a mixed metallic, covalent and ionic bonding state. To determine the change of the bonding character, starting at TaC ending at TaN, density of states (DOS) calculations were performed for the fully occupied crystal structures. Strong covalent bonding is indicated by a strong overlap of Ta d-orbital and C p-orbital, respectively [30]. Figure 2a reveals, that this especially holds for pure TaC, plotting the

projected DOS. When substituting carbon atoms with nitrogen, the Ta-d DOS in the p-band lowers ($TaC_{0.75}N_{0.25}$), indicating reduced amounts of covalent bonds [31] and starts to broaden between N and C p-orbital with more N added ($TaC_{0.5}N_{0.5}$ and $TaC_{0.25}N_{0.75}$). In agreement increases the DOS at the $N(E_F)$ for nitrogen richer TaC_xN_{1-x}, highlighting a more metallic bonding character. At this point we need to mention, that for TaN the wavy curve at the Fermi level, $N(E_F)$, is maybe be inaccurate. The contribution of ionic bonding is linked to the charge transfer between Ta and C/N atoms. Lavrentyev et al. show that a charge transfer increases for $TaC_{0.5}N_{0.5}$, thus leading to an increase of ionic bonding [32]. In summary, the computational data suggest a more ductile character for Ta-C-N compared to Ta-C – increasing Pugh ratio and Couchy pressure as well as a more metallic bonding character within the DOS. -

To proof our theoretical observations, we also conducted standard analysis, e.g. XRD and SEM, of the deposited $Ta_{0.47}C_{0.34}N_{0.19}$ coating. XRD measurements revealed a strong 110 texture of the film, indicated by a single peak at the corresponding 2 theta value. In addition, SEM analysis highlighted a very dense and smooth, columnar structure – coating thickness of about 900 nm. This observation was confirmed by TEM investigations – see Figure 3. Selected Area Electron Diffraction (SAED) analysis as well as Fast Fourier Transformation (FFT) of high resolution images showed patterns corresponding to a (110) oriented film (see Figure 3a). The lattice constant determined from SAED yields to 4.43±0.03 Å, being exactly between the two calculated values for the different potentials used, and hence in excellent agreement (see Appendix). Bright field imaging nicely shows the dense and columnar structure as also observed during SEM investigations (see Figure 3b). Together with dark field images the mean width of these columns is estimated to be around 34±10 nm, representing relatively large values compared to polycrystalline films [10]. However, as shown in Figure 3c, using inverse FFT of masked spots, one could visualize lattice planes highlighting many dislocations present in the film. Furthermore, no significant amorphous phase fractions was detected during TEM investigations. Standard nanoindentation measurements obtained hardness values of 43.3±1.4 as well as indentation modulus of 569±24 GPa, respectively. The hardness exceeds the already reported values for Ta-C-N [10] and can be explained by higher compressive stresses within the film, utilizing increased bias potentials, as well as a slight influence of the substrate material utilized.

In general, pillars of two different diameters and aspect ratios were prepared for the compression tests. Aspect ratios of h/D of about 1.0 as well as 1.6 were chosen due to size limitations of the film thickness. Based on the weakness of the substrate, we investigated two different heights to rule out the influence of e.g. sink-in effects. This results in pillars with height equal the film thickness (D) as well as with 0.55·D. Wheeler and Michler [33] proposed that for calculating the yielding stress, the smallest cross-sectional area needs to be used for tapered pillars. Therefore, the engineering stress-strain curve and corresponding yielding stress (σ_Y) – presented in Figure 4– are calculated using the top diameter of the pillars. It should be mentioned that the pillar surface was not perfectly flat, obtaining slightly rounded edges. We therefore decided to use the mean value of the upper and lower diameter of the edges and identified these two boundaries as an error bar. The mean error is measured to be ±11 nm. Taking this into account, the error in measuring the diameter due to the shape of the pillar is considered the main failure for the strain-stress curves. The strain-error due to the substrate deformation was accounted by using Sneddon's correction [34] – see equation 1.

$$\Delta L_{Sneddon} = \frac{(1-\nu_{sub}^2)}{E_{sub}} \frac{F}{d} \qquad (1)$$

In equation 1, ν_{sub} and E_{sub} refer to the Poisson's ratio and Young's modulus of the sapphire substrate, F denotes the applied force and d the contact diameter between pillar and substrate. Figure 4a gives representative stress/strain curves for each diameter and aspect ratio with the corresponding pictures of the pillars after compression (Figure 4c to e – aspect ratio of 0.94, 1.08, and 1.63, respectively). Pillars with a smaller aspect ratio obtain clearly reduced slopes. This is in accordance with FEM simulations and pillar compression tests performed by I. Choi et al. [35]. Furthermore, they show that the apparent Young's modulus for small aspect ratios is much smaller than the theoretical ones. This gives an idea why the slope is smaller compared to what we would expect from the calculations. However, in this work we are more focused on the plastic behavior and therefore go in no further details on the deviation of the expected Young's modulus. The initial upward bending of the curve is a sign of a slight misalignment of the flat punch and the pillar surface [36]. In consequence the apparent linear portion of the elastic regime of the stress-strain curve decreases with increasing tilting angle. The bending is especially apparent for the pillar with an aspect ratio of 1.63. We determined the yielding stress using the intersection of the linear slope of the elastic and plastic regime, respectively. The results, depicted in Figure 4b, do not show any size dependence of the yield strength neither influence of the substrate. The mean yield stress

σ_Y of all compressed pillars is 16.89 ±1.39 GPa. Furthermore, the mean value of the stress of the first maximum from all tested pillars is 19.48 ± 0.98 GPa. Strain bursts during compression occurred at a stress of around 18.75±0.74 GPa. Within all curves in Figure 4b we clearly see that after the yielding point a region is followed with plastic deformation accompanied by a further increase in stress. Also, small "bumps" in the stress – strain curve can be seen in this regime indicating minor slip events occurring in the pillar. Especially, pillars with no single slip, but several small ones show this behavior. The columns seen in these pillars exceed the mean columnar width (34±10 nm), but are associated with the morphology of the film. After a stress decrease a major shear event occurs. This strain burst happens very abrupt so that the tip jumps down quickly although it is operated in displacement mode. We observed this strain burst for every pillar except for some of the 500 nm diameter and 0.9 aspect ratio. There is not one major step, but a series of small shear events observed. Furthermore, keeping the compression after the first burst we could induce another burst showing the same stress-strain behavior as before. When comparing the change of pillar height before and after compression from SEM images, with the collected displacement data from the indenter, we see that the final strain is overestimated by around 1-2 %. Furthermore, for some curves with a strain burst there is an additional difference of 2-3 % in strain. We relate this with inaccuracy of the indenter due to the abrupt change of displacement during the bursts. Strain bursts have been observed by several works on micro compression tests including also the one conducted by Uchic [14], which are associated with dislocation avalanches of highly stochastic nature. They have mostly appeared in single crystals, whereas in polycrystalline materials a reduction of these strain bursts replaced by a lot of very small "avalanches" is observed [37].

The SEM images of the compressed pillars showing major slip events (Figure 4b to d) for the {111} slip plane, which seems to be the most active one – based on the angle. This determination is possible due to the uniform (110) orientation of the columnar grains. Hence, {111} plane is the densest packed plane in a fcc crystal and usually associated with a dense packed direction as the slip direction would be $<01\bar{1}>$. We therefore suggest {111} $<01\bar{1}>$ as the active slip system. Furthermore, we estimated the resolving shear stress within the slip system. Applying Schmid's law, $\tau = m \cdot \sigma$, with m being the Schmid factor (0.408), the shear stress at the Yield point is around 6.86 GPa. With the calculated shear modulus of 185 GPa the shear stress refers to G/27. At the first peak (σ=19.48 GPa) it would come down to G/23. Simulations predict that the stress sufficient for dislocation nucleation is dependent on the

surface geometry. Therefore, small steps in the surface enable dislocation nucleation at stresses between G/10 and G/20 at 0 K [38]. Extrapolating the stress at the first peak at room temperature to 0 K the obtained value is in the range for dislocation nucleation [39]. This highlights the possibility that deformation not only occurs through dislocation flow but also through dislocation nucleation.

The setup for fracture toughness tests of single cantilever beam bending and pillar splitting is depicted in Figure 5a and b, respectively. The initial bending of the cantilever before loading is due to the high compressive stress within the film. The small load drops in load-displacement curves of the single cantilever bending tests (see Figure 6a) can be associated with bridging ligaments of the pre-crack or be indicative for plasticity effects [1]. They do not change the slope significantly and are therefore considered to have minor influence. Furthermore, the curves plotted in Figure 6a are strongly dependent on the actual cantilever dimension, which explains the big variation in slope and critical load Figure 6. We have to mention that the cantilever thickness exceeds the thin film thickness up to about 100 nm and therefore a non-assessable influence of the base material is present. In addition, a beam cross-section of 1x1 µm² is considered to be the minimum for this test set up which is slightly undercut by these beams. Fracture toughness was calculated from the tests according to a commonly used equation described by Brinckmann et al. [40]:

$$K_{IC} = \frac{Fl}{wh^{3/2}} f\left(\frac{a}{h}\right) \qquad (2)$$

Whereby $f\left(\frac{a}{h}\right)$ is a geometry factor [40], a, denotes the crack length, h, the beam height, w, the beam width, l, the beam length, and F, the critical load where the beam fails. The mean value of K_{IC} was determined to be 2.9±0.25 MPa·m$^{1/2}$ (mean value estimated out of 7 cantilevers). The most commonly used material systems for protective coatings, Ti-N and Ti-Al-N, exhibit stress intensity factors of about 1.9 and 2.7±0.3 MPa·m$^{1/2}$, respectively – applying the same testing method [41]. Furthermore, a test on non-textured $TaC_{0.81}$ yielded about 1.79 MPa·m$^{1/2}$ – further details on the synthesis can be found in [42]. However, stress intensity factor, K_{IC}, from pillar splitting tests is calculated from the critical load (P_c), where the pillar fails, the pillar radius, R, and a dimensionless coefficient, γ, based on the E/H ratio.

$$K_{IC} = \gamma \cdot \frac{P_c}{R^{1.5}} \qquad (3)$$

M. Ghidelli et al. [43] calculated, γ, using cohesive zone finite element modeling for different indenter angles and E/H ratios. Nanoindentation measurements of the film give an E/H ratio of 13.14. According to their study, using a cube corner tip for pillar indentation, leads to γ = 0.7. Load-displacement curves of pillar splitting tests are shown in Figure 6b. Using the smallest radius at the pillar top, K_{IC} = 7.12±0.8 MPa·$m^{1/2}$. This significantly exceeds the fracture toughness obtained from single cantilever beam testing. Therefore, deficiencies of the performed pillar splitting tests have to be considered. First a 200nm cube corner tip on a 950nm wide pillar makes an accurate positioning rather difficult, if not impossible. Yet off-centered indentation leads to an underestimation of K_{IC} [44]. Secondly, for smaller pillars the ion dose due to FIB milling leads to slight overestimation of K_{IC}. In addition, indentation depth exceeds with about 300 nm (33% of thin film thickness) the 10 % rule for nanoindentation ensuring no influence of the substrate. Furthermore, γ is calculated for an ideal isotropic elastic material [19]. Columnar grained structure as well as an anisotropy ratio of 0.56 are major deviations for this assumption. Simulations for single cantilever beam bending tests on the other hand have shown that material anisotropy only has a minor influence and can maybe neglected [40].

In general fracture toughness measured by pillar splitting is considered to be slightly higher than measured by cantilever techniques [19]. However, the source of huge difference obtained in this work could not be explained in-detail and only estimated by the listed deficiencies. But the independency of cantilever bending tests on crystal anisotropy allows a direct comparison between the tested polycrystalline $TaC_{0.81}$ and oriented $TaC_{0.64}N_{0.36}$ film. This implies that the theoretical predicted ductility enhancement with nitrogen indeed enhances fracture toughness. This is further strengthened by the comparison with TiN and the enormous stress intensity factor gained from the pillar splitting tests.

Conclusion

In summary, we investigated the mechanical properties of Ta-C-N using various micromechanical testing methods. Based on semi-epirical criteria – Pugh ratio and Cauchy pressure – obtained from DFT calculations, suggest an increased damage tolerance by substituting carbon with nitrogen atoms. $Ta_{0.47}C_{0.34}N_{0.19}$ was therefore synthesized as highly

(110) textured thin film using reactive magnetron sputtering. Despite super-hardness (43.3±1.4 GPa), we observed plastic deformation over a yield stress σ_Y of 16.89 ±1.39 GPa in micro-pillar compression tests. We clear proofed plastic deformation, due to major shear deformation along the most active {111} <$01\bar{1}$> slip plane. In addition, single cantilever bending tests result in a stress intensity factor, K_{IC}, of 2.9±0.25 MPa·$m^{1/2}$ whereas pillar splitting tests suggest K_{IC}=7.12±0.8 MPa $m^{1/2}$. As a comparative use of different micromechanical tests is essential, the substitution of carbon by nitrogen within the highly brittle Ta-C system forming Ta-C-N indeed enhances ductility and fracture toughness.

Acknowledgement

We thank the Vienna Scientific Cluster for the attribution of computation time, the X-ray center of TU Wien for beam time, the USTEM center of TU Wien for the SEM and TEM facilities, as well as the collaboration and generous support of Prof. S. Kodambaka and his group.

Figure captions

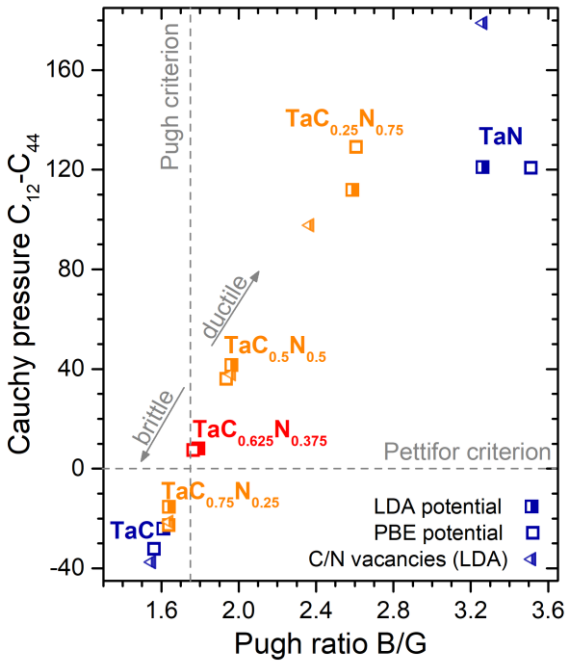

Figure 1: Empirical criteria for ductile/brittle material behavior. Open and half-filled symbols depict PBE and LDA potential, respectively. Triangles represent defected cell with carbon and nitrogen vacancies (6 %). $TaC_{0.625}N_{0.375}$ (red) was further investigated experimentally.

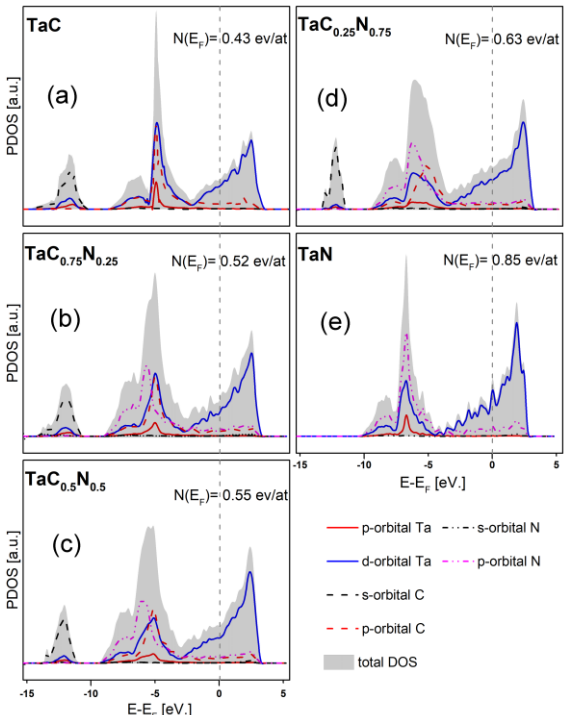

Figure 2: Evolution of DFT calculated projected density of states from TaC to TaN.

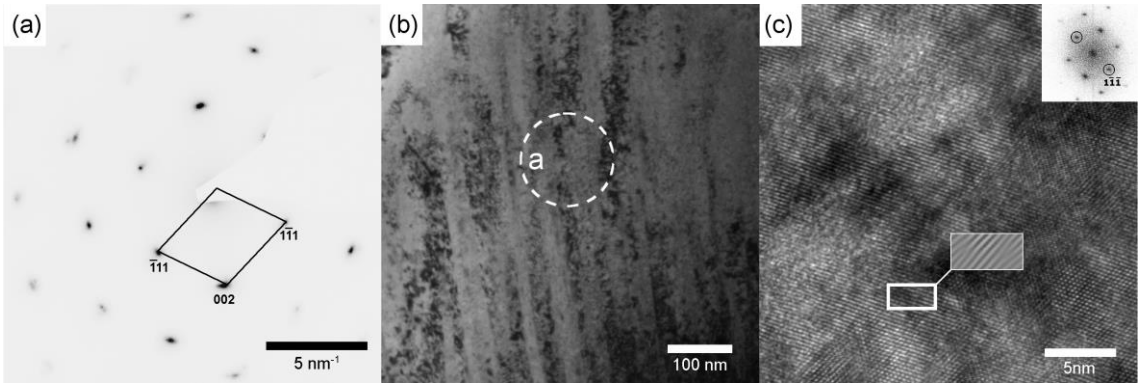

Figure 3: Cross-sectional TEM analysis of $Ta_{0.47}C_{0.34}N_{0.19}$ showing (a) SAED with ZA=[110], (b) bright field image with indicated SA-aperture and (c) high resolution image. Upper corner inset depicts a fast Fourier transformation (FFT) of the image. The inset in the middle depicts an inverse FFT of the $(1\bar{1}\bar{1})$ peaks showing dislocations in the framed area.

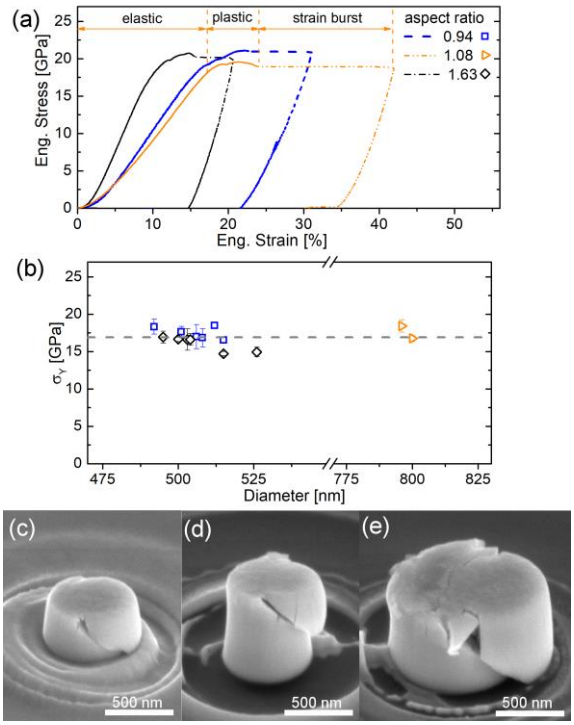

Figure 4: Micro-pillar compression tests performed for different diameters and aspect ratios. (a) Engineering stress-strain curves calculated using the smallest diameter of the pillars. Elastic, plastic regime as well as strain burst are indicated for pillar (e). (b) Yield stress where plastic deformation of the pillars starts. (c-e) Pillars after compression with aspect ratio of 0.94 (c), 1.63 (d) and 1.08 (e).

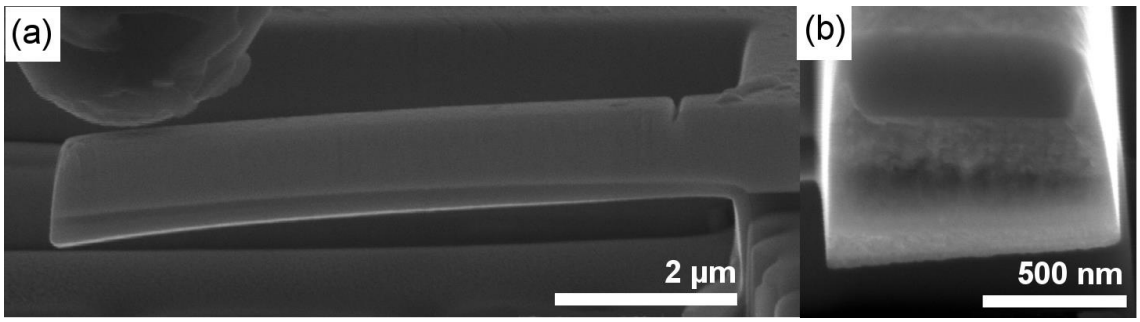

Figure 5: (a) Single cantilever beam bending test configuration and (b) fractured area for K_{IC} evaluation.

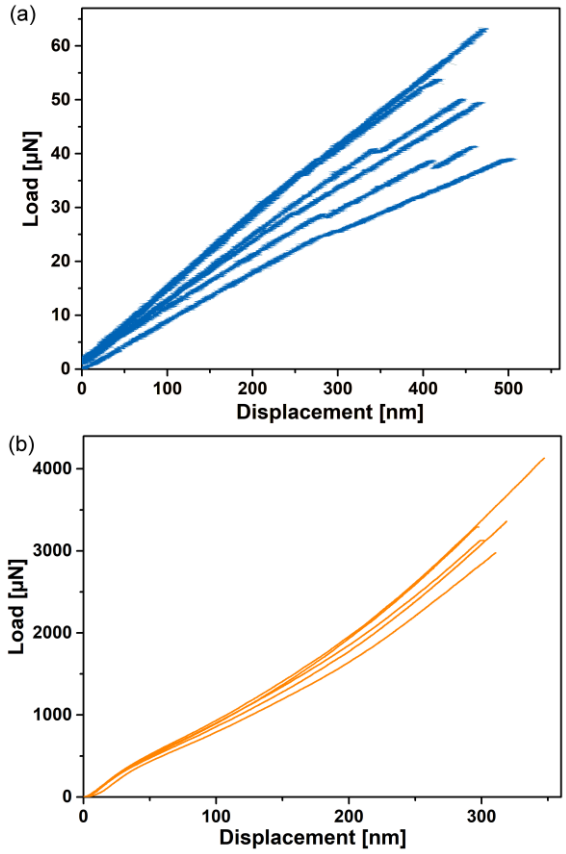

Figure 6: Load-displacement curves for single cantilever bending (a) and pillar splitting tests (b).

Appendix

Table 2: $TaC_{0.625}N_{0.375}$ DFT calculations using two different exchange correlation potential approximations, PBE and LDA. Table shows lattice constant (a), elastic constants of stiffness tensor (C_{11} C_{12} C_{44}), G, B, E moduli (in GPa), Poisson's ratio (v) and Pugh's ratio (B/G) and Cauchy pressure C_{11}-C_{44}.

	X	a	C_{11}	C_{12}	C_{44}	G	B	E	v	B/G	C_{11}-C_{44}
PBE	0.625	4.468	635	148	141	176	310	443	0.26	1.76	7.43
LDA	0.625	4.402	737	158	149	195	350	494	0.26	1.79	8.15

References

[1] W.M. Seidl, M. Bartosik, S. Kolozsvári, H. Bolvardi, P.H. Mayrhofer, Vacuum 150 (2018) 24–28.

[2] R. Bermejo, R. Daniel, C. Schuecker, O. Paris, R. Danzer, C. Mitterer, Adv. Eng. Mater. 19 (2017).

[3] R. Hahn, M. Bartosik, R. Soler, C. Kirchlechner, G. Dehm, P.H. Mayrhofer, Scr. Mater. 124 (2016) 67–70.

[4] M. Bartosik, R. Hahn, Z.L. Zhang, I. Ivanov, M. Arndt, P. Polcik, P.H. Mayrhofer, Int. J. Refract. Met. Hard Mater. 72 (2018) 78–82.

[5] V. Moraes, H. Riedl, C. Fuger, H. Bolvardi, P. Polcik, D. Holec, P.H. Mayrhofer, Submitt. to Sci. Reports (2018).

[6] O. Cedillos-Barraza, D. Manara, K. Boboridis, T. Watkins, S. Grasso, D.D. Jayaseelan, R.J.M. Konings, M.J. Reece, W.E. Lee, Sci. Rep. 6 (2016) 37962.

[7] W.S. Williams, Prog. Solid State Chem. 6 (1971) 57–118.

[8] H. Riedl, T. Glechner, T. Wojcik, N. Koutná, S. Kolozsvári, V. Paneta, D. Holec, D. Primetzhofer, P.H. Mayrhofer, Scr. Mater. 149 (2018) 150–154.

[9] D.J. Rowcliffe, G.E. Hollox, J. Mater. Sci. 6 (1971) 1261–1269.

[10] T. Glechner, S. Kolozsvári, S. Fritze, E. Lewin, V. Paneta, D. Primetzhofer, D. Holec, P.H. Mayrhofer, H. Riedl, (2018).

[11] H. Leiste, M. Stüber, V. Schier, H. Holleck, Mater. Sci. Forum 308–311 (1999) 467–475.

[12] H. Holleck, V. Schier, Surf. Coatings Technol. 76–77 (1995) 328–336.

[13] H. Holleck, H. Schulz, Surf. Coatings Technol. 36 (1988) 707–714.

[14] M.D. Uchic, Science (80-.). 305 (2004) 986–989.

[15] G. Dehm, B.N. Jaya, R. Raghavan, C. Kirchlechner, Acta Mater. 142 (2018) 248–282.

[16] S. Kiani, C. Ratsch, A.M. Minor, J. Yang, S. Kodambaka, Scr. Mater. 100 (2015) 13–16.

[17] H. Lasfargues, T. Glechner, C.M. Koller, V. Paneta, D. Primetzhofer, S. Kolozsvári, D. Holec, H. Riedl, P.H. Mayrhofer, Surf. Coatings Technol. 309 (2017) 436–444.

[18] W.C. Oliver, G.M. Pharr, J. Mater. Res. 7 (1992) 1564–1583.

[19] M. Sebastiani, K.E. Johanns, E.G. Herbert, F. Carassiti, G.M. Pharr, Philos. Mag. 95 (2015) 1928–1944.

[20] G. Kresse, J. Furthmüller, Phys. Rev. B 54 (1996) 11169–11186.

[21] G. Kresse, D. Joubert, Phys. Rev. B 59 (1999) 1758–1775.

[22] W. Kohn, L.J. Sham, Phys. Rev. 140 (1965) A1133–A1138.

[23] J.P. Perdew, K. Burke, M. Ernzerhof, Phys. Rev. Lett. 77 (1996) 3865–3868.

[24] S.-H. Wei, L.G. Ferreira, J.E. Bernard, A. Zunger, Phys. Rev. B 42 (1990) 9622–9649.

[25] R. Yu, J. Zhu, H.Q. Ye, Comput. Phys. Commun. 181 (2010) 671–675.

[26] D.G. Pettifor, Mater. Sci. Technol. 8 (1992) 345–349.

[27] S.F. Pugh, London, Edinburgh, Dublin Philos. Mag. J. Sci. 45 (1954) 823–843.

[28] R. Hill, Proc. Phys. Soc. Sect. A 65 (1952) 349–354.

[29] F. Tasnádi, M. Odén, I.A. Abrikosov, Phys. Rev. B - Condens. Matter Mater. Phys. 85 (2012) 1–9.

[30] M. Sahnoun, C. Daul, M. Driz, J.C. Parlebas, C. Demangeat, Comput. Mater. Sci. 33 (2005) 175–183.

[31] K. Schwarz, 8436 (2017).

[32] A.A. Lavrentyev, B. V Gabrelian, V.B. Vorzhev, I.Y. Nikiforov, O.Y. Khyzhun, 472 (2009) 104–111.

[33] J.M. Wheeler, J. Michler, Rev. Sci. Instrum. 84 (2013) 45103.
[34] I.N. Sneddon, Int. J. Eng. Sci. 3 (1965) 47–57.
[35] I. Choi, Y. Gan, D. Kaufmann, O. Kraft, R. Schwaiger, J. Mater. Res. 27 (2012) 2752–2759.
[36] Y.S. Choi, M.D. Uchic, T.A. Parthasarathy, D.M. Dimiduk, Scr. Mater. 57 (2007) 849–852.
[37] J.R. Greer, J. Th, M. De Hosson, Prog. Mater. Sci. 56 (2011) 654–724.
[38] J. Godet, S. Brochard, L. Pizzagalli, P. Beauchamp, J.M. Soler, Phys. Rev. B - Condens. Matter Mater. Phys. 73 (2006) 1–4.
[39] S. Liu, J.M. Wheeler, J. Michler, X.T. Zeng, W.J. Clegg, 117 (2016) 24–27.
[40] S. Brinckmann, C. Kirchlechner, G. Dehm, Scr. Mater. 127 (2017) 76–78.
[41] M. Bartosik, C. Rumeau, R. Hahn, Z.L. Zhang, P.H. Mayrhofer, Sci. Rep. 7 (2017) 16476.
[42] H. Riedl, T. Nguyen, T. Wojcik, T. Glechner, S. Kolozsvári, V. Paneta, D. Holec, D. Primetzhofer, P.H. Mayrhofer, Unpublished (n.d.).
[43] M. Ghidelli, M. Sebastiani, K.E. Johanns, G.M. Pharr, J. Am. Ceram. Soc. 100 (2017) 5731–5738.
[44] C.M. Lauener, L. Petho, M. Chen, Y. Xiao, J. Michler, J.M. Wheeler, Mater. Des. (2018).

5 Concluding remarks

The Ta-C-N system shows very interesting properties regarding the modification of the binary systems, Ta-C in particular. Through the introduction of vacancies, especially Ta vacancies the solid solution of Ta-C and Ta-N can be extended to high nitrogen contents. Therefore, single phase Ta-C-N can be synthesized over a wide range using PVD with its pronounced introduction of structural defects, such as vacancies. On the cost of weakening of the bonding strength through the substitution of carbon with nitrogen atoms resulting in a decrease of hardness and a decreased high temperature phase stability, ductility of the brittle Ta-C can be enhanced. Furthermore, Publication I highlights the retained hardness for Ta-C-N up to 1000 °C. Publication II yields a more detailed insight to this discovery. There the decrease of bonding strength is correlated with a decrease of the covalent and an increase of the metallic bonding portion. A highly textured thin film was synthesized with a composition near the brittle to ductile behavior boarder proposed by calculations of the empirical ductility measure Pugh ratio and Cauchy pressure and furthermore, analyzed using widely used micromechanical testing methods. Plastic deformation was observed in micro-pillar compression testing with {111} <$1\bar{1}0$> as the active slip system. Superior fracture toughness of Ta-C-N compared to Ta-C was confirmed by single cantilever bending tests and pillar splitting.

Summing up this work highlights the adaption of thermomechanical properties through a substitution of interstitial atoms and thus changing of the interatomic bonding. In optimizing the deposition parameters super hard Ta-C-N thin films can be gained which are temperature stable up to at least 1000 °C and exhibit enhanced ductility compared to Ta-C. This outcome may open new perspectives for the development of next generation high temperature stable protective coatings.